Electrochimica Acta 388 (2021) 138556

Contents lists available at ScienceDirect

Electrochimica Acta

journal homepage: www.elsevier.com/locate/electacta

Novel ($CH_6N_3^+$, NH_3^+)-functionalized and nitrogen doped Co_3O_4 thin film electrochemical sensor for nanomolar detection of nitrite in neutral pH

Ariel Ndala[a], Bamato Itota[a], Jessica Chamier[b], Sekhar Ray[c], Christopher Sunday[a], Mahabubur Chowdhury[a,*]

[a] Department of chemical engineering, Cape Peninsula University of Technology, Bellvile, 7535, South Africa
[b] HySA Catalysis, Department of Chemical Engineering, University of Cape Town, Rondebosch 7700, South Africa
[c] Department of Physics, CSET, University of South Africa, Florida, 1709, South Africa

ARTICLE INFO

Article history:
Received 1 March 2021
Revised 28 April 2021
Accepted 3 May 2021
Available online 18 May 2021

Keywords:
Nitrite detection
Nitrogen doping
Amino acid functionalisation
Co_3O_4
Electrochemical sensor
L-Arginine

ABSTRACT

The present work provides a soft chemical route for simultaneous nitrogen doping and ($CH_6N_3^+$, NH_3^+)-functionalization of pre-deposited Co_3O_4 thin film. The Co_3O_4 thin film was prepared by metal-organic decomposition (MOD) on fluorine-doped tin oxide (FTO) substrate and hydrothermally treated in the presence of amino acid, L-Arginine. The L-Arginine-treated Co_3O_4 thin film (L-Arginine/Co_3O_4/FTO) was used for the electrochemical detection of nitrite under neutral pH condition. Various physical (i.e. XRD, XPS, SEM, and Raman spectroscopy) and electrochemical characterization (i.e. CV, CA, EIS, and Tafel slope) was conducted to elucidate the role and effect of L-Arginine on Co_3O_4 film and determine the sensor performance characteristics. L-Arginine/Co_3O_4/FTO electrode exhibited a low limit of detection of 1.95 nM, an ultrafast response time of <2 s, and a wide linear range of up to 16 mM in neutral pH. The sensor was nitrite selective in the presence of common interferants and showed chemical stability and reproducibility. The practical application of the proposed sensor was demonstrated using real samples for nitrite detection.

1. Introduction

Nitrite is predominantly used as corrosion inhibitor [1], bleaching agent [2], and food additive [3]. Recently, researchers have reported the environmental risks [4] and health implications [5] of human exposure to elevated concentrations of nitrite. The World Health Organization (WHO) has set the maximum limit of nitrite in drinking water at 65 µM [6]. Quantitative analysis of nitrite is therefore necessary for quality control using an adequate detection method. Various techniques for the determination of nitrite, including chromatography [7], catalytic-spectrophotometry [8], chemiluminescence [9], and so forth have been implemented. These methods require expensive instrumentation and skilled personnel to operate. Electrochemical techniques are cost-effective, simple, effective and favour highly sensitive and selective detection of nitrite [10].

Owing to their small size (1 – 100 nm), conductivity, and chemical reactivity, nanomaterials have been widely used in catalysis [11] and sensors [12]. Over the past two decades, scientists have developed a panel of electrochemical nitrite sensors using carbon [13], enzymes [14], metals [15], metal oxides [16], and polymers [17] as modifiers. Among the metal oxide modifiers, cobalt oxide (Co_3O_4) is of interest in this study because of its mixed valance state, availability, chemical stability, high electrocatalytic activity, selectivity, and extensive application in different areas of research and industry, such as catalysis [18], lithium batteries [19], and sensors [20]. Spinel Co_3O_4, written as $Co^{2+}[Co^{3+}]_2O_4^{2-}$, contains Co^{2+} and Co^{3+} ions located each in the tetrahedral and octahedral sites, respectively [21]. Tuning the ratio of Co^{3+}/Co^{2+} provides the means to tailor reactive properties of cobalt oxide [22]. Also, the synthetic approach of cobalt oxide materials has profound influence on their performance [23]. Electrodeposition [24], atomic layer deposition [25], and plasma sputtering [26] are among the numerous preparation methods for the direct growth of Co_3O_4 nanomaterials on conductive substrates. However, the non-uniformity of the plated material in electrodeposition, and high vacuum requirement in atomic layer deposition and plasma sputtering have prompted the chemical solution deposition of Co_3O_4 [27] on substrates for catalytic oxidation processes. Based on dif-

* Corresponding author.
E-mail address: chowdhurym@cput.ac.za (M. Chowdhury).

https://doi.org/10.1016/j.electacta.2021.138556
0013-4686/

ferent film morphology requirements, three variants of chemical solution deposition technique, i.e., sol-gel method, chelate process, and metal-organic decomposition (MOD) can be distinguished [28]. Of these three methods, MOD is the simplest as no precise control over hydrolysis and condensation is needed during growth of nanoparticles. The technique has been widely used for the synthesis of ferroelectric materials [29]. To improve their electronic conductivity and extend their application for sensors, MOD-grown thin films of doped Co_3O_4 have been synthesized recently for the detection of biomarkers, such as glucose [30]. However, the doping method used in these studies was limited to the incorporation of cationic impurities into the cobalt oxide precursor solution, and the possibility of altering the surface properties of MOD-synthesized Co_3O_4 thin films was not explored. Recently, Plasma-assisted nitrogen doping of MOD-synthesized CuO/Cu_2O thin film has been achieved and the beneficial role of nitrogen doping in glucose sensing was highlighted [31]. However, plasma-assisted surface treatment requires high vacuum equipment, which increases capital cost.

Several efforts have been made to functionalize metal oxide surfaces by organic ligands to improve their electrochemical performance for sensing applications [32]. Yet, most of those organic ligands used for surface functionalization are toxic and possess only one type of functional groups. Amino acids are eco-friendly, benign and have both amino and carboxyl groups in their molecular structure. These desirable characteristics, among others, have promoted research activities in amino acid-functionalized metal oxides [33]. L-Arginine is an attractive surface modifier as it is green, non-toxic, water soluble, and its side chain (guanidinium, $pK_A = 12.5$) has a delocalized positive charge which remains protonated over a wide pH range [34]. The delocalized positive charge on the guanidino group of L-arginine enables the formation of multiple hydrogen bonds and has favoured the use of guanidinium-bearing molecules as anion receptors [35]. The nitrogen content in L-Arginine molecule is 32.1 % (w/w), which makes L-Arginine a nitrogen-rich source for chemical doping [36]. Recently, Li and co-authors [37] confirmed the electron doping of a MoS_2 monolayer (n-type semiconductor) using Arginine. In other words, the amino acid induced n-type functionalization of the MoS_2 monolayer. The modified MoS_2 monolayer showed good performance as field effect transistor (FET). Bora and co-authors [38] have converted an undoped hematite film into faceted superstructures with excellent photocurrents after hydrothermal treatment of the film in aqueous solution of $FeCl_3{\bullet}6H_2O$ and L-Arginine. However, Bora and co-authors, like others [39], only highlighted the role of L-Arginine as a size and morphology director of nanostructures during the hydrothermal reaction. Moreover, the possibility of L-Arginine dissociation during hydrothermal treatment and its effect on the chemical and physical properties of the material were not analysed in depth.

In this study, we have successfully ($CH_6N_3^+$, NH_3^+)-functionalized and nitrogen-doped a pristine MOD-derived Co_3O_4 thin film in one-pot hydrothermal treatment with L-Arginine. We have provided spectral evidence that simple hydrothermal treatment can lead to oxygen vacancy and nitrogen atoms (dissociated from L-arginine) can compete for substitution in Co_3O_4 crystal lattice. This technique can serve as a new platform for element doping and surface functionalization of metal oxides post deposition for various sensing applications. To the best of our knowledge, this is the first study to show that: a) hydrothermal treatment of Co_3O_4 thin film in the presence of L-Arginine can alter the physico-electrochemical properties of the film by simultaneous surface functionalization and nitrogen doping and b) the functionalized and nitrogen-doped Co_3O_4 thin film exhibits enhanced electrochemical behaviour towards nitrite detection in neutral pH.

2. Experimental

2.1. Materials

All reagents were purchased from Sigma-Aldrich South Africa and used without further purification. All chemicals were reagent grade. A phosphate buffer (PBS) with a concentration of 0.1 M and a pH of 7.4 was used as electrolyte and wash buffer. Deionized water (DI) was used throughout the experiment.

2.2. Co_3O_4 Electrode fabrication

Co_3O_4 thin film was prepared by using methods reported in literature [33, 34, 40]. In a typical synthesis, cobalt oleate was prepared by ion exchange reaction between cobalt (II) chloride hexahydrate and sodium oleate as previously reported [42]. An amount of 0.126 g of cobalt oleate was dispersed into 0.7 mL of toluene. The mixture was sonicated for 45 min in a 45 kHz ultrasonic bath for homogeneity. Three pre-cleaned and cut-to-size FTO slides (geometric area = 1 cm^2) were spin-coated each at 4000 rpm for 1 min with 50 µL of the homogeneous cobalt oleate solution prior to calcination at 350 °C for 10 min. The spin coating and calcination of the slides were repeated alternately until four layers of deposition were reached. XRD data confirms the presence of Co_3O_4 crystal structure (Fig S1 electronic supplementary document) without any other phase presents of the as prepared Co_3O_4 thin film as reported by our earlier work [41].

2.3. Hydrothermal treatment of Co_3O_4

One of the three Co_3O_4 modified FTO slides, labelled Co_3O_4/FTO, was stored in pristine condition, and the other two were hydrothermally treated each with a different reacting medium at 90 °C for 24 h in a Teflon-lined stainless-steel autoclave. HT-Co_3O_4/FTO and L-Arginine/Co_3O_4/FTO were formed after treatment with 60 mL water and 60 mL of 0.15 M L-Arginine solution (pH = 11), respectively. Various concentrations of L-Arginine were used, however, 0.15 M L-Arginine resulted in the best performing electrode in terms anodic peak current (Data not shown). The hydrothermally treated electrodes were washed repeatedly with PBS and dried at room temperature overnight. The resulting slides, i.e., Co_3O_4/FTO, HT-Co_3O_4/FTO, and L-Arginine/Co_3O_4/FTO were physically and electrochemically characterized thereafter. The complete fabrication process is summarized in Scheme 1.

2.4. Electrochemical evaluation

All electrochemical measurements were carried out using Autolab PGSTAT302N potentiostat. The conventional three-electrode setup was adopted in which Ag/AgCl (3 M KCl) acted as the reference electrode, Pt as counter electrode, and the as prepared electrodes as working electrode. Cyclic voltammetry (CV) experiments were performed in 0.1 M PBS solution (pH = 7.4) in the presence of 2 mM NO_2^- at a scan rate of 10 mV/s. The electrochemical impedance study was conducted at room temperature, at the ac voltage amplitude of 10 mV, and within the frequency range of 0.01–10^5 Hz in 0.1 M KCl + 5 mM $K_3[Fe(CN)_6]$ solution. The Randles equivalent circuits were obtained using EIS Spectrum Analyser in Newton algorithm mode.

2.5. Physical characterization

SEM micrographs of the surface texture of Co_3O_4/FTO, HT-Co_3O_4/FTO, and L-Arginine/Co_3O_4/FTO were obtained by using Tescan MIRA3 RISE SEM, a high-resolution Field Emission SEM combining low kV imaging Nova NanoSEM. Raman spectra for

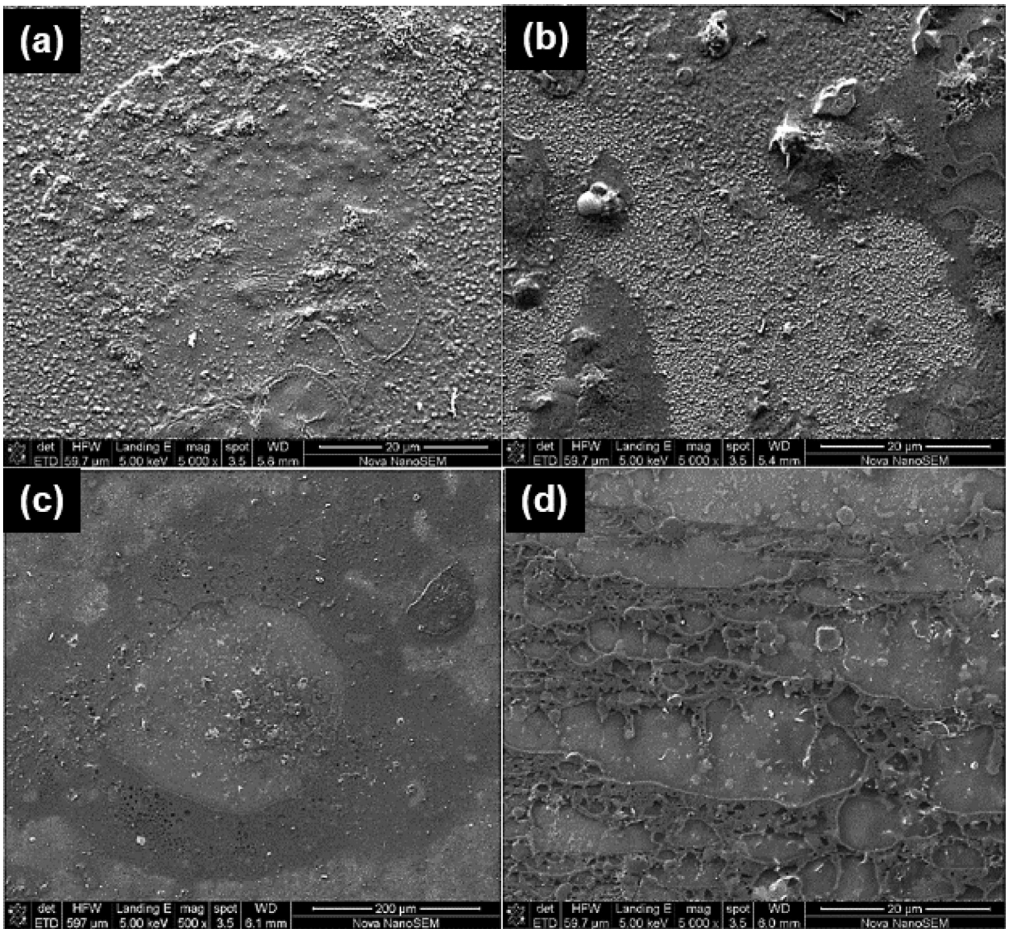

Fig. 1. SEM images of (a) Co_3O_4/FTO, (b) HT-Co_3O_4/FTO, (c) L-Arginine/Co_3O_4/FTO thin films, and (d) Magnified view of (c).

Co_3O_4/FTO, HT-Co_3O_4/FTO, and L-Arginine/Co_3O_4/FTO were obtained by using the Witec Confocal Raman Microscope (alpha300). The XPS measurements were carried out on Co_3O_4/FTO, HT-Co_3O_4/FTO, and L-Arginine/Co_3O_4/FTO with spatial resolution of < 3 µm using KRATOS AXIS X-ray photoelectron spectrometer at UNISA (Florida Science Campus), South Africa.

3. Results and discussion

3.1. Physical characterization

The as prepared electrodes, i.e., Co_3O_4/FTO, HT-Co_3O_4/FTO, and L-Arginine/Co_3O_4/FTO were characterized using SEM, Raman spectroscopy, and XPS. It can be seen from SEM images that there is no change in the rough and compact surface of pristine Co_3O_4/FTO (Fig. 1a) after hydrothermal treatment (HT-Co_3O_4/FTO thin film in Fig. 1b). However, the hydrothermal treatment of pristine Co_3O_4/FTO thin film in the presence of L-Arginine (Fig. 1c & d) caused a drastic modification of its surface texture. The difference in surface structure between HT-Co_3O_4/FTO and L-Arginine/Co_3O_4/FTO arises through chelation of cobalt oxide surface by the amino acid in basic environment (pH = 11), causing the dissolution of some cobalt from the electrode surface into adsorbate solution. This is consistent with the depleted cobalt content in L-Arginine/Co_3O_4/FTO, as per XPS analysis in Table S1 (electronic supplementary document). The porous nature of the surface of L-Arginine/Co_3O_4/FTO can potentially allow easy access to active sites and improve mass transport kinetics.

Fig. 2a shows five Raman-active modes of Co_3O_4/FTO thin film at 192(F_{2g}), 470(E_g), 514(F_{2g}), 605 (F_{2g}), and 674(A_{1g}) cm^{-1}, which compare well with those of pure Co_3O_4 [43]. Hence, the Raman-active modes as detected confirm the presence of spinel Co_3O_4 structure. The Raman-active bands for HT-Co_3O_4/FTO and L-Arginine/Co_3O_4/FTO thin films are narrower and appear at higher wavenumbers than those for Co_3O_4/FTO, highlighting a decrease in oxygen vacancies [44]. However, the A_{1g} line for L-Arginine/Co_3O_4/FTO is significantly blue shifted. Previous studies reported the unusual upshift of A_{1g} mode as a sensitive indication of heteroatomic doping [45]. In this case, the formation of a Co-N bond is plausible after hydrothermal treatment of Co_3O_4/FTO in L-Arginine environment since the amino acid is a potential nitrogen source. The additional upshifts of $F_{2g} + E_g + F_{2g} + F_{2g}$ modes for L-Arginine/Co_3O_4/FTO compared with those for HT-Co_3O_4/FTO may be the result of nitrogen incorporation into Co_3O_4 lattice. Because N (ionic radius of N^{3-} = 1.46 Å) is bigger than O (ionic radius of O^{2-} = 1.36 Å), substitutional N doping can cause compressive forces to the lattice near N^{3-} (i.e., Co-O), thereby reducing the mean bond length of Co-O bond and increasing its vibration frequency. Thus, the more significant shift of A_{1g} mode for L-Arginine/Co_3O_4/FTO suggests that N substituted O in octahedral coordination, since the site in the vicinity of N^{3-} experiences stronger squeezing forces than that further away. No other phases were detected in the Raman spectra for Co_3O_4/FTO, HT-Co_3O_4/FTO, and L-Arginine/Co_3O_4/FTO, as shown in Fig. 2a. The enhancement in Raman emission for HT-Co_3O_4/FTO could be the result of hole doping after exposure of Co_3O_4/FTO to hole-donors, such as hydroxyl groups (-OH) in the hydrothermal medium [46].

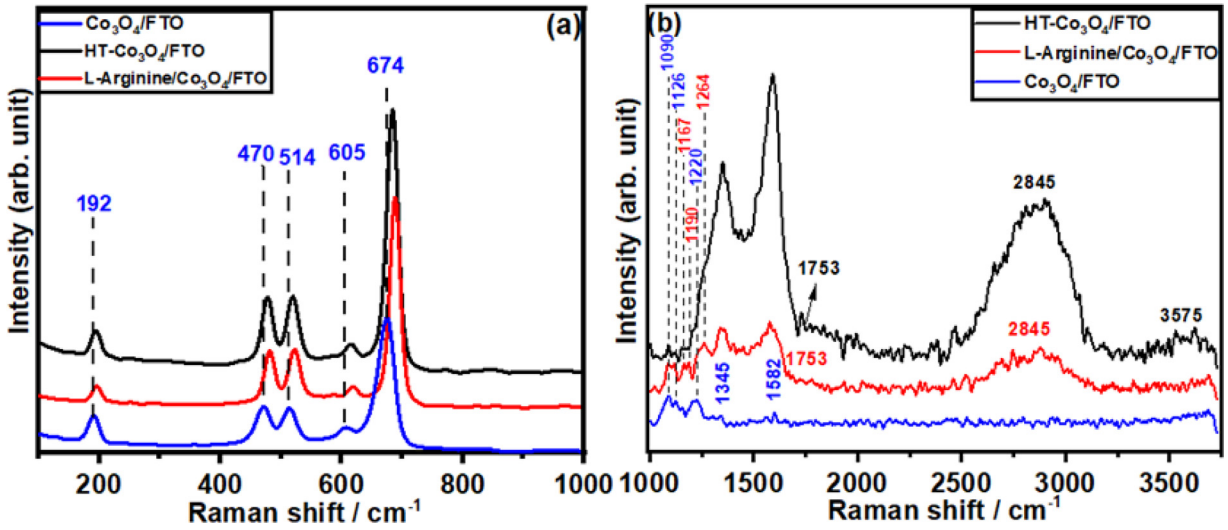

Fig. 2. Raman spectra for Co_3O_4/FTO, HT- Co_3O_4/FTO, and L-Arginine/ Co_3O_4/FTO thin films within wavenumber ranges of (a) 100 – 1000 cm^{-1} and (b) 1000 – 3750 cm^{-1}.

The increased hole content in HT-Co_3O_4/FTO can promote high field emission properties. The hole doping effect is, however, less acute in the Raman spectrum for L-Arginine/Co_3O_4/FTO certainly because of the amino groups introduced by the amino acid, which can act as electron-donors.

In Fig. 2b, the Raman peaks for Co_3O_4/FTO, HT-Co_3O_4/FTO, and L-Arginine/Co_3O_4/FTO at 1090, 1119/1126, 1220, 1345/1582 cm^{-1} are ascribed to C-O(H), asymmetric aliphatic C=O, C-O-C, and C-C bond, respectively [83], accounting for adventitious carbon during the preparation procedure and carbon from the oleate precursor. The broad bands (one small and the other strong) at 1753 cm^{-1} and 2845 cm^{-1} are attributed, respectively, to the Raman stretching of carboxylic C=O and alcoholic or carboxylic -OH involved in hydrogen bonding interactions [47, 48]. The weak broad band at 3575 cm^{-1} can be assigned to the hydrogen bonded hydroxyl group of water molecule [49]. The peak around 1190 cm^{-1} is attributed to stretching vibration of CO group of the amino acid molecule [50]. It is worth mentioning that this peak (1190 cm^{-1}) is less intense and occurs at lower frequencies (by 2-3 cm^{-1}) than that in the cited literature. This could mean coordination of L-Arginine to Co_3O_4 surface. The Raman signals at 1167 cm^{-1} and 1264 cm^{-1} are also signatures, respectively, of NH_3^+ rocking [51] and Cδ-twist [52] in the amino acid.

All the XPS spectra (C 1*s*, O 1*s*, Co 2*p*, and N 1*s*) were referenced at 284.8 eV for adventitious carbon and deconvoluted using OriginPro software. C 1*s* and O 1*s* can be viewed in Figures S2 and S3 (electronic supplementary document), respectively.

It is important to stress out that we only considered Co $2p_{3/2}$ (Fig. 3a - d) for spectral deconvolution as usually reported for Co_3O_4 [53]. Co $2p_{3/2}$ XPS main peak for Co_3O_4/FTO can be seen at 779.1 eV, with a spin orbit splitting (Co $2p_{1/2}$ –Co $2p_{3/2}$) of 15.1 eV as confirmation of mixed Co (II and III) in Co_3O_4 [23]. The XPS peak at 779.1 eV is assigned to low coordinated octahedral Co^{3+} whereas the peak at 780.1 eV is ascribed to low coordinated tetrahedral Co^{2+}. These two peaks appear at lower binding energies (by 0.4 eV) than expected [54] due to higher electron density resulting from oxygen vacancies . The peak area ratio of octahedral Co^{3+} to tetrahedral Co^{2+} (Co^{3+}/Co^{2+}) for Co_3O_4/FTO was calculated to be 2.27, which is in good agreement with recently published results [55]. The XPS signals at 780.8/782.4 and 781.8 eV are attributed, respectively, to Co^{2+} [56] and Co^{3+} [57] at the surface or subsurface. The two satellite peaks at 784 eV and 788.3 eV are associated with paramagnetic Co^{2+} [58]. Notable XPS spectral changes can be observed for HT-Co_3O_4/FTO in Fig. 3(d) with respect to the spectrum for Co_3O_4/FTO. In particular, the blueshift (by 0.2 eV) of Co $2p_{3/2}$ main peak (779.3 eV), consequently the lower spin-orbit spacing (14.9 eV) for HT-Co_3O_4/FTO suggests an increase in Co^{3+} content due to oxygen filling. To confirm this, we further calculated the Co^{3+}/Co^{2+} ratio (2.70) and found it to be higher than that for Co_3O_4/FTO. When oxygen fills the vacancy (forward direction of Equation 1), it introduces partially filled 2*p* orbitals that drive out the two electrons trapped in cationic sites (this is reflected by the upshift of Co 2*p* XPS main peak and increase in Co^{3+} concentration) then becomes completely filled (O^{2-}).

$$Co^{2+} - V_O - Co^{2+} + {}^1/_2O_2 \leftrightarrow Co^{3+} - O^{2-} - Co^{3+} \quad (1)$$

The higher Co^{3+}/Co^{2+} ratio can also be linked to an increased amount of hole in HT-Co_3O_4/FTO since Co^{3+} has one electron less than Co^{2+} in its electronic configuration. The hole doping has an enhancing effect on the photoemission of Co 2*p* XPS spectrum for HT-Co_3O_4/FTO. These observations affirm the oxidation of Co^{2+} to Co^{3+} took place after oxygen filling of Co_3O_4/FTO during treatment with water. Based on Sensor and Electrochemical Characterizations (following section), the performance of Co_3O_4/FTO for nitrite detection at neutral pH seems to decrease with an increase in Co^{3+} concentration, suggesting Co^{2+} as the active site for nitrite electrooxidation in neutral PBS solution.

In contrast, decomposition of Co$2p_{3/2}$ XPS spectrum for L-Arginine/Co_3O_4/FTO reveals the presence of a metallic phase of cobalt (Co^0) at 778.8 eV as proof of Co-N bond formation [59] which corroborates the Raman and O1s XPS. The Co-N bond formation has been reported to promote metallic conductivities [60] and may be responsible for the superior electrochemical activity of L-Arginine/Co_3O_4/FTO towards nitrite oxidation compared with Co_3O_4/FTO and HT- Co_3O_4/FTO. The ratio of $[(Co^0+Co^{3+})/Co^{2+}]$ was found to be 2.14 which is close to that of Co^{3+}/Co^{2+} 2.27 for Co_3O_4/FTO suggesting partial substitution of oxygen in octahedral coordination by nitrogen. Co $2p_{3/2}$ XPS main band (779.5 eV) for L-Arginine/Co_3O_4/FTO, with a spin-orbit splitting of 14.6 eV, experiences a much larger blueshift than that for HT-Co_3O_4/FTO. Also, a higher A/B ratio can be observed in Fig. 3a for L-Arginine/Co_3O_4/FTO compared with that for HT-Co_3O_4/FTO and Co_3O_4/FTO. These spectral behaviours assuredly stem from the presence of doping N atoms in L-Arginine treated Co_3O_4 lattice. Explicitly, similarly to oxygen filling, nitrogen filling of oxygen vacancies can unleash two electrons from the 3*d* states of two Co(II)

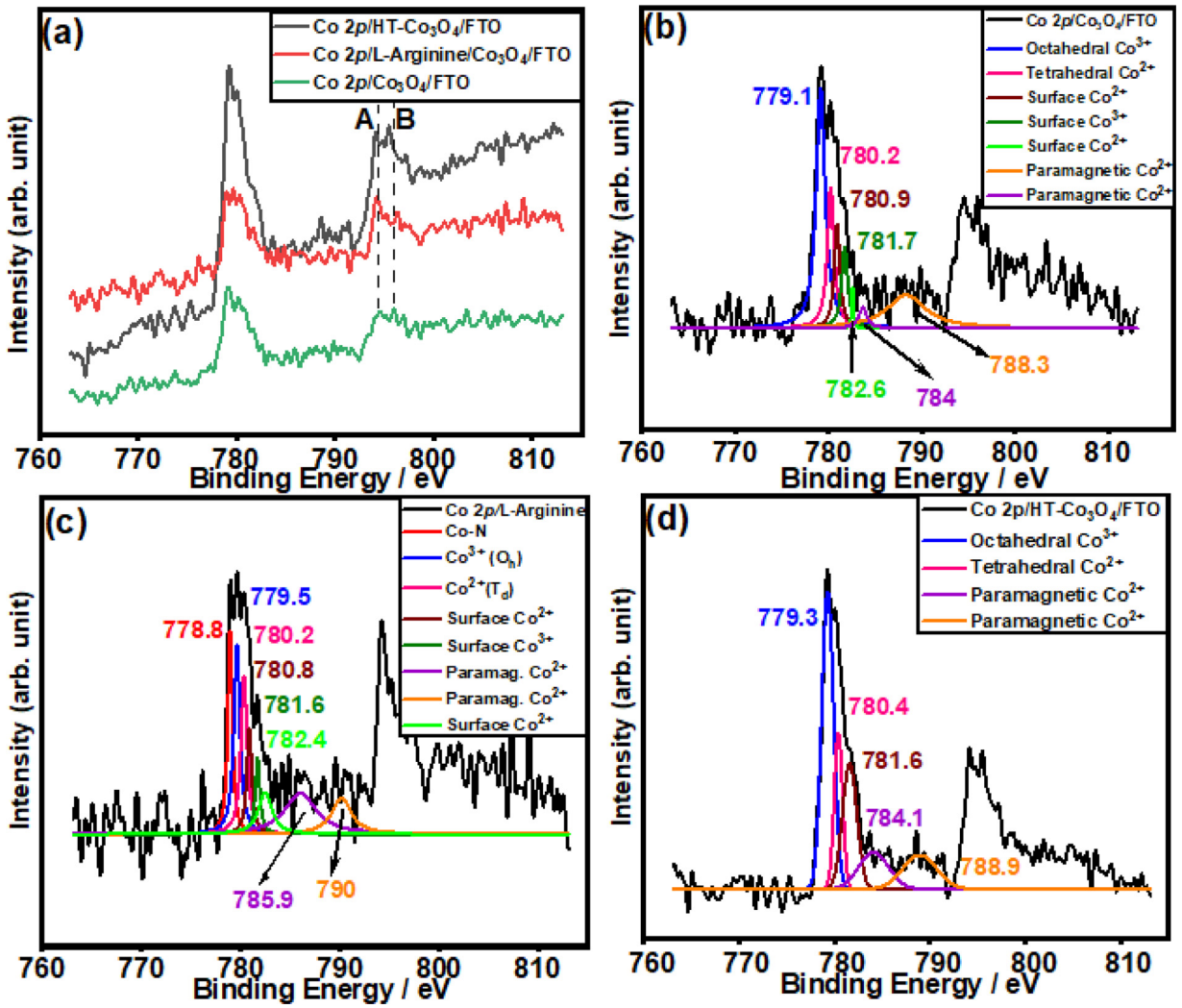

Fig. 3. a) Co 2p XPS spectral peaks for Co_3O_4/FTO, HT- Co_3O_4/FTO, and L-Arginine/ Co_3O_4/FTO thin films. Lorentzian and Gaussian Co 2p XPS peaks for b) Co_3O_4/FTO, c) L-Arginine/ Co_3O_4/FTO and d) HT- Co_3O_4/FTO.

cations, forming N^{2-}. However, as opposed to O^{2-}, N^{2-} has one unfilled 2*p* orbital and can cause additional electron transfer from the 3*d* orbitals of most likely Co(II) (it is easier to eject an electron from Co(II) than Co(III)) to produce N^{3-} species, as illustrated by Equation 2-3.

$$Co^{2+} - V_O - Co^{2+} + {}^1/_2N_2 \rightarrow Co^{3+} - N^{2-} - Co^{3+} \quad (2)$$

$$Co^{3+} - N^{2-} - Co^{3+} + - Co^{2+} - \rightarrow Co^{3+} - N^{3-} - Co^{3+} + - Co^{3+} - \quad (3)$$

While substitutional nitrogen doping of Co_3O_4 will cause a redshift of Co $2p_{3/2}$ XPS peak center [61], nitrogen filling the oxygen vacancies will induce its blueshift [62]. Therefore, the observed giant upshift of the Co $2p_{3/2}$ XPS main line for L-Arginine/Co_3O_4/FTO was proposed to be the result of the synergistic effect of nitrogen and oxygen filling.

To further understand the role of L-Arginine, the N1s XPS spectrum for L-Arginine/Co_3O_4/FTO was evaluated to confirm the presence of L-Arginine on Co_3O_4 surface (Fig. 4a and c). The deconvoluted spectrum showed peaks at 398.6, 399.2, 399.7, 400.4, and 401.5 eV, as seen in Fig. 4c. The peak at 398.6 eV was ascribed to Co-N bond [63] while the peaks at 399.2 and 401.5 eV were assigned to coordinated (or basic) α-amine group [64] and protonated (or acidic) α-amine group [65], respectively. The high ratio of basic α-amine to acidic α-amine ($N/N^+ = 4.1$) confirmed the coordination of L-Arginine α-amine group to Co_3O_4. Coupling Co 2*p* and N1s XPS results with Raman spectroscopic study for L-Arginine/Co_3O_4/FTO, coordination of the amino acid to Co_3O_4 through carboxylate and α-amine groups was established. We assigned the photoemission at 400.4 eV (which would appear at 400.6 eV if C 1*s* were referenced at 285 eV) to the guanidinium group of L-Arginine with delocalized positive charge on the three nitrogen atoms [66], but the area ratio of unprotonated α-amine group to guanidinium group was calculated to be 1:2, significantly lower than the stoichiometric value of 1:3. This led to the conclusion that some molecules of L-Arginine were decomposed via their side chains, of which the decomposition product was the nitrogen dopant. The protonated guanidinium on the surface of L-Arginine/Co_3O_4/FTO can increase its affinity for negatively charged species. The binding energy peak at 399.7 eV was attributed to chemically adsorbed dinitrogen (N_2) [67], which can also be observed at 399.8 eV in Fig. 4b. The presence of highly oxygenated nitrogen species was also noticed near 409 eV in the N1s XPS spectrum for L-Arginine/Co_3O_4/FTO in Fig. 4a. Hence, it can be postulated that the decomposition pathway of L-Arginine is similar to the hydrolysis of methylguanidine, reported in [68]. Hence, the nitrogen doping mechanism was proposed in Scheme 2.

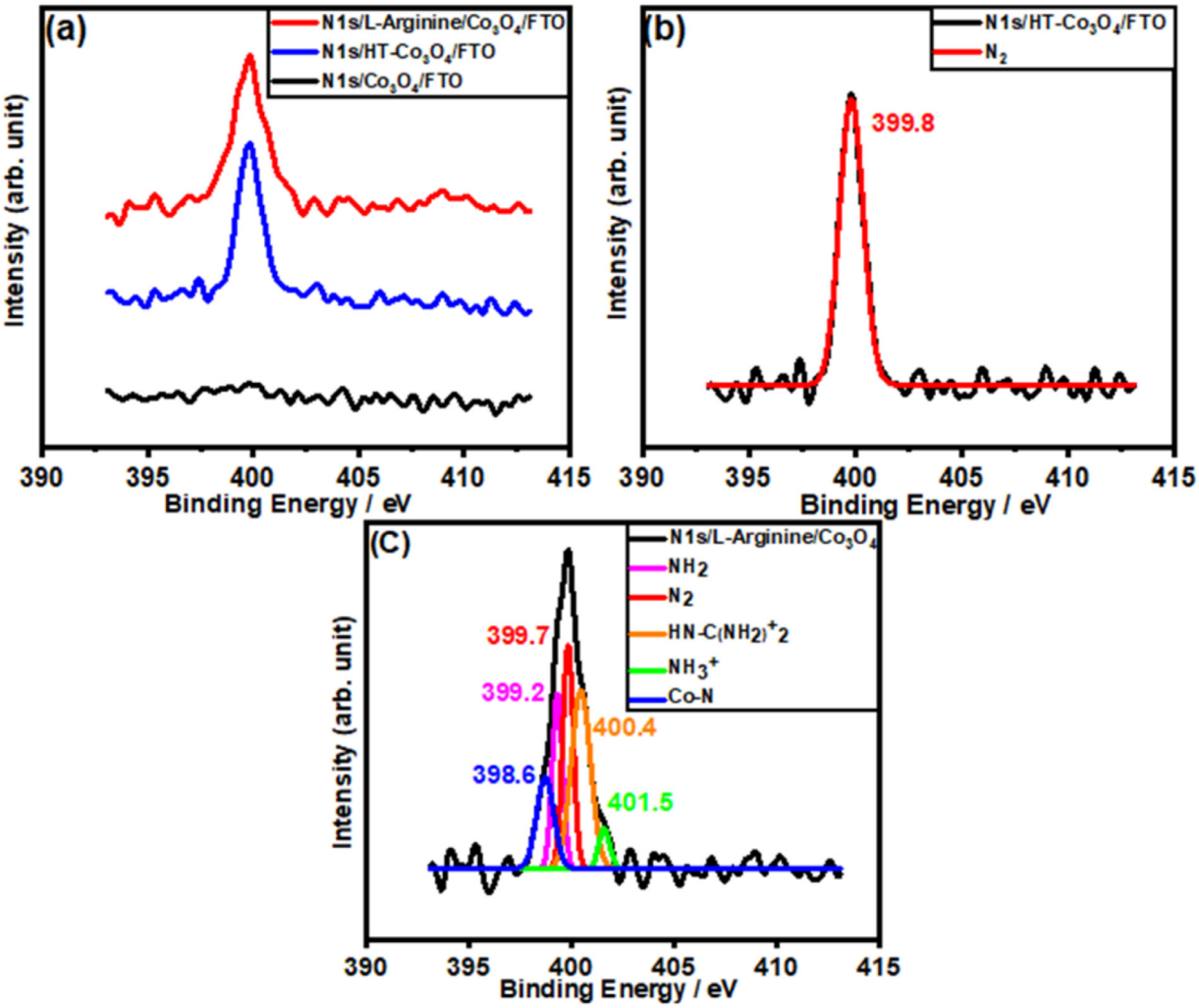

Fig. 4. a) N1s XPS spectral emissions for Co_3O_4/FTO, HT- Co_3O_4/FTO, and L-Arginine/ Co_3O_4/FTO thin films. Gaussian N1s XPS peaks; b) HT- Co_3O_4/FTO, and (c) L-Arginine/ Co_3O_4/FTO.

A summary of the binding energy peak positions for the Co 2*p* XPS analysis of each electrode and their respective peak assignments is presented in Table S2 (electronic supplementary document). The spectral weight ratio results of O1s and Co $2p_{3/2}$ XPS for the three electrodes are presented in Table S3 (electronic supplementary document).

3.2. Electrochemical behaviour of the as prepared electrodes

3.2.1. Cyclic voltammetry studies of the as prepared electrodes

Cyclic voltammograms (CV) in Fig. 5a show the electrochemical response of the various electrodes to 2 mM NO_2^-. The L-Arginine/Co_3O_4/FTO electrode exhibited the best electrochemical activity, i.e., the highest anodic peak current response centered at 0.989 V compared to other electrodes studied. The enhanced CV response of L-Arginine/Co_3O_4/FTO towards nitrite oxidation is favoured by its metallic conductivity resulting from nitrogen doping after hydrothermal treatment of Co_3O_4/FTO with L-Arginine as was shown from XPS analysis. Also, the surface modification with cationic functional groups can possibly induce preconcentration effect on nitrite followed by a sharp increase of anodic peak current density [69]. These highlight the role of L-Arginine as a nitrogen doping source and surface functionalizing agent.

A reversible redox reaction near the nitrite oxidation peak potential was observed on the L-Arginine/Co_3O_4/FTO electrode in the absence of nitrite (Fig. 5b). The reversible peak can be attributed to the Co(II)/Co(III) redox couple, according to the following equation [70]:

$$Co_3O_4 + H_2O + OH^- \rightarrow 3CoOOH + e \quad (4)$$

No current response (Fig. 5a) was observed for bare FTO and L-Arginine/FTO in nitrite suggesting the absence of a redox-active species, i.e., Co_3O_4.

The various scan rate study was conducted to determine the nature of the electrode process at L-Arginine/Co_3O_4/FTO in the presence of nitrite. As presented in Fig. 6a, the anodic and cathodic peak currents increased with increasing sweep rate in the range of 10-200 mVs^{-1}. Particularly, the oxidation peak current varied linearly with the square root of scan rate (Fig. 6b) as is the case with a diffusion-controlled process [71]. Some nitrite adsorption on L-Arginine/Co_3O_4/FTO surface was confirmed by Fig. 6c showing the nearly linear relationship between anodic peak current density and scan rate.

It can be seen from Fig. 6d that the peak potentials increase with scan rate ($\log\nu$), which suggests that nitrite electrooxidation at L-Arginine/Co_3O_4/FTO is chemically irreversible [72]. The anodic transfer coefficient (α_a) can be derived from the equation given by [72]:

$$E_{pa} = I + \frac{2.303RT}{2(\alpha_a)n_aF}\log(v) \quad (5)$$

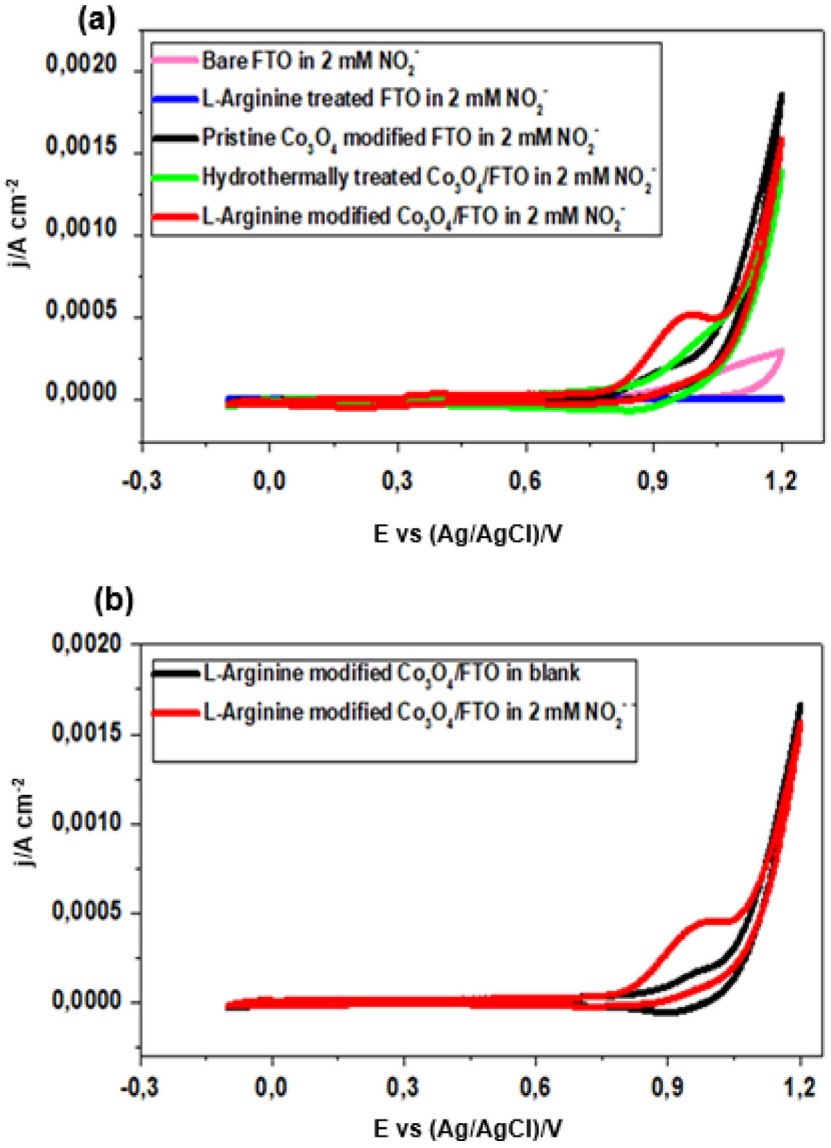

Fig. 5. a) CV for the electrooxidation of 2 mM nitrite in 0.1 M PBS (pH = 7.4) at 10 mVs^{-1} and b) CV of L-Arginine/Co_3O_4/FTO in the presence and absence of 2 mM nitrite.

Where E_{pa} is the anodic peak potential (V), I is the E_{pa}-intercept (V), R is the ideal gas constant (8.314 J/mol.K), T is room temperature (298 K), v is the scan rate (mVs^{-1}), and n_a is the number of electrons involved in the rate-determining step, F is the Faraday constant (96500). After mathematical treatment of Equation 5, a value of 0.31 was found for $(\alpha_a)n_a$. The value of $\alpha_a = 0.31$ (< 0.5) suggests that the activation barrier is on the reactant (reduced species) side. Alternatively, in the absence of a plot of E_{pa} against log(v), α_a can be easily estimated from a cyclic voltammogram using Matsuda's equation [73]. Hence, in case of Co_3O_4/FTO (0.883) and HT-Co_3O_4/FTO (0.619), α_a was determined by Matsuda:

$$E_p - E_{p/2} = \frac{0.0477}{(\alpha_a)n_a} \tag{6}$$

Where E_p and $E_{p/2}$ are the oxidation peak and half-peak potentials (V), respectively, obtained from Fig. 5a. α_a for L-Arginine/Co_3O_4/FTO, HT-Co_3O_4/FTO, and Co_3O_4/FTO was used for the calculation of the heterogeneous electron transfer rate constant (k^0). The k^0 values for L-Arginine/Co_3O_4/FTO, HT-Co_3O_4/FTO, and Co_3O_4/FTO were calculated using Equation (7) as given below [74]:

$$I = E^{0'} + \frac{RT}{(\alpha_a)n_aF} \times \left\{0.78 + \left(\frac{2.3}{2}\right)\log\left[\frac{(\alpha_a)n_aFD}{(k^0)^2RT}\right]\right\} \tag{7}$$

Where, $E^{0'}$ is the formal electrode potential (V), estimated here from the cyclic voltammograms in Fig. 5a using the procedure described in [75], and D is the diffusion coefficient of nitrite (1.7×10^{-5} cm^2/s) [13]. A faster electron transfer process, corresponding to a 50 % increase, occurs at L-Arginine/Co_3O_4/FTO electrode (k^0 = 0.00172 cm/s) compared to pristine Co_3O_4/FTO (k^0 = 0.00116 cm/s) and HT-Co_3O_4/FTO electrode (k^0 = 0.00113 cm/s). This highlights the superior electrochemical activity of the L-Arginine/Co_3O_4/FTO electrode compared to other electrodes studied.

The nitrite sensing capability of L-Arginine/Co_3O_4/FTO was determined in the concentration range from 2 to 19 mM NO_2^- and is shown in Fig. 7a. The oxidation peak current response of L-Arginine/Co_3O_4/FTO was linearly (R^2 = 0.99) proportional to the nitrite concentration in PBS solution within the investigated range Fig. 7b. Furthermore, progressive positive shifts of the anodic peak potential with increasing ana-

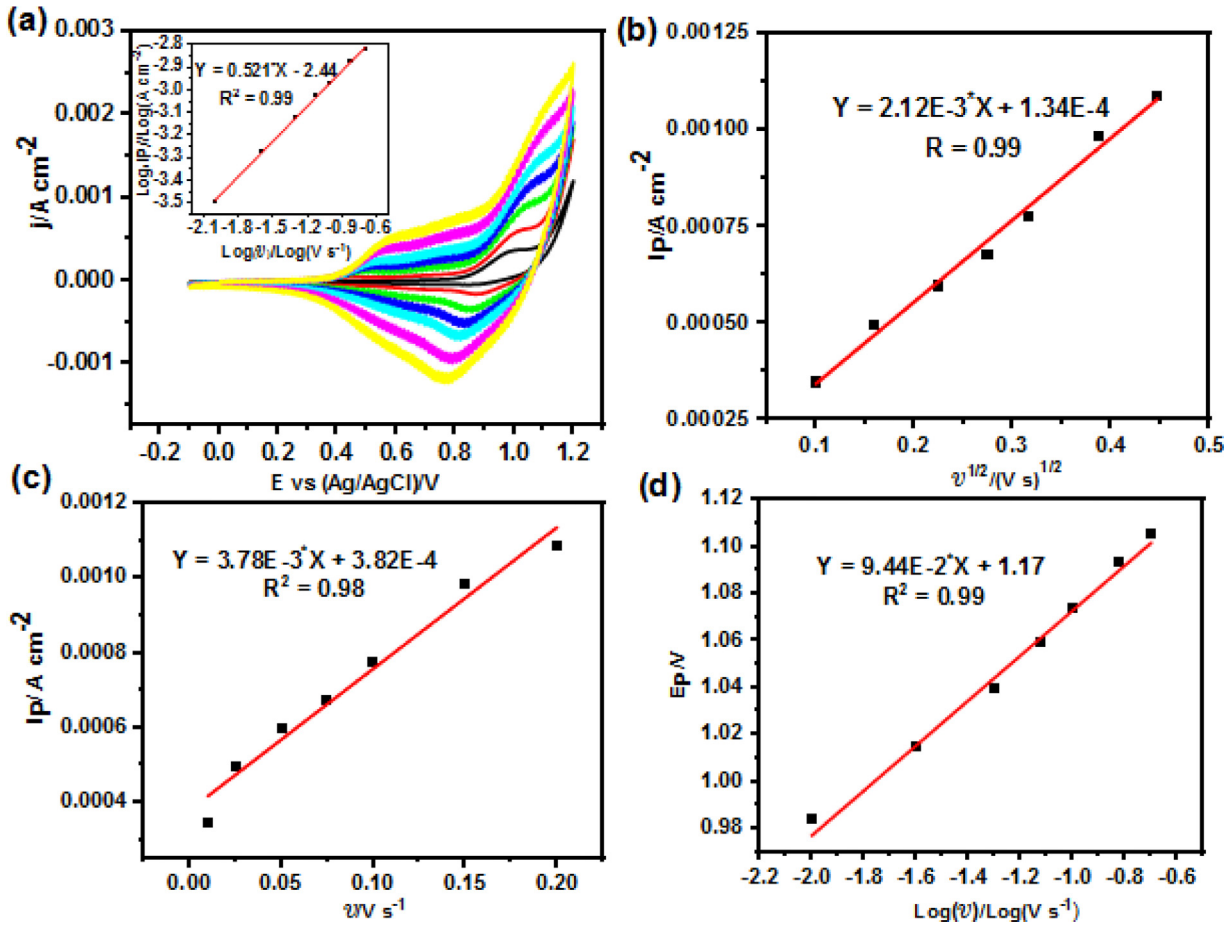

Fig. 6. a) Cyclic voltammograms of L-Arginine/Co_3O_4/FTO in 2 mM nitrite and 0.1 M PBS (pH = 7.4) at various scan rates (10, 25, 50, 75, 100, 150, and 200 mVs^{-1}). Inset graph shows a logarithmic plot of anodic peak current vs scan rate; b) anodic peak current density vs square root of scan rate; c) anodic peak current density vs scan rate, and (d) anodic peak potential vs logarithm of scan rate.

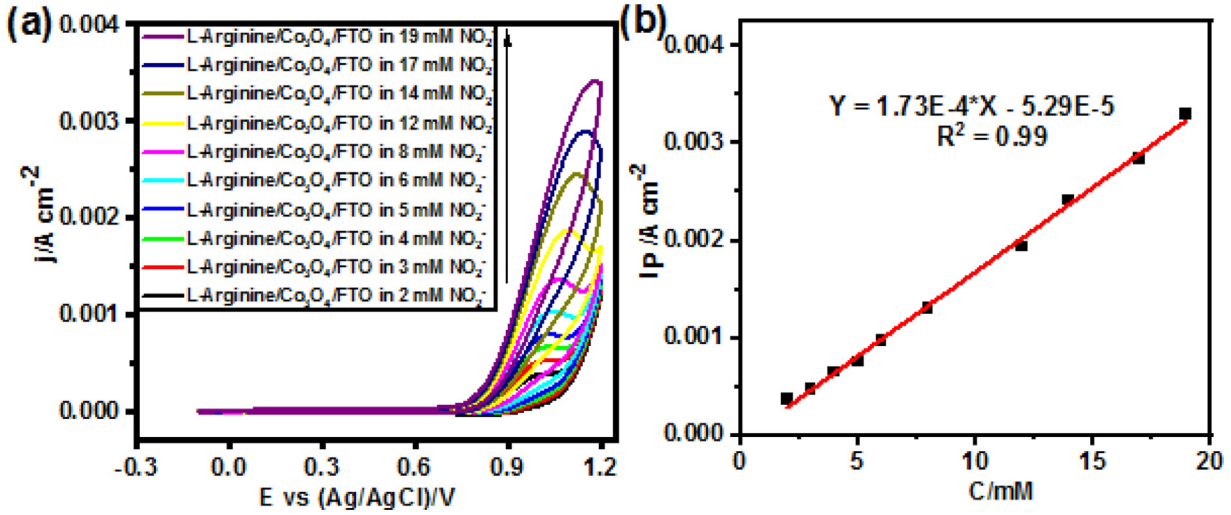

Fig. 7. a) Cyclic voltammograms for L-Arginine/Co_3O_4/FTO in the presence of 2 – 19 mM nitrite in 0.1 M PBS (pH = 7.4) at 10 mVs^{-1}. (b) Plot of oxidation peak current density vs nitrite concentration.

lyte concentration were detected. This phenomenon occurs due to analyte adsorption on the electrode surface as mentioned earlier. Each binding event, due the interaction between nitrite and L-Arginine/Co_3O_4/FTO, establishes a new activation overpotential [76].

3.2.2. Electrochemical impedance spectroscopy study of the as prepared electrodes

Electrochemical impedance spectroscopy (EIS) was used to further evaluate the electron transport kinetics of the L-Arginine/Co_3O_4/FTO, HT-Co_3O_4/FTO and Co_3O_4/FTO electrodes. Corresponding Nyquist spectra are presented in Fig. 8a. The Nyquist

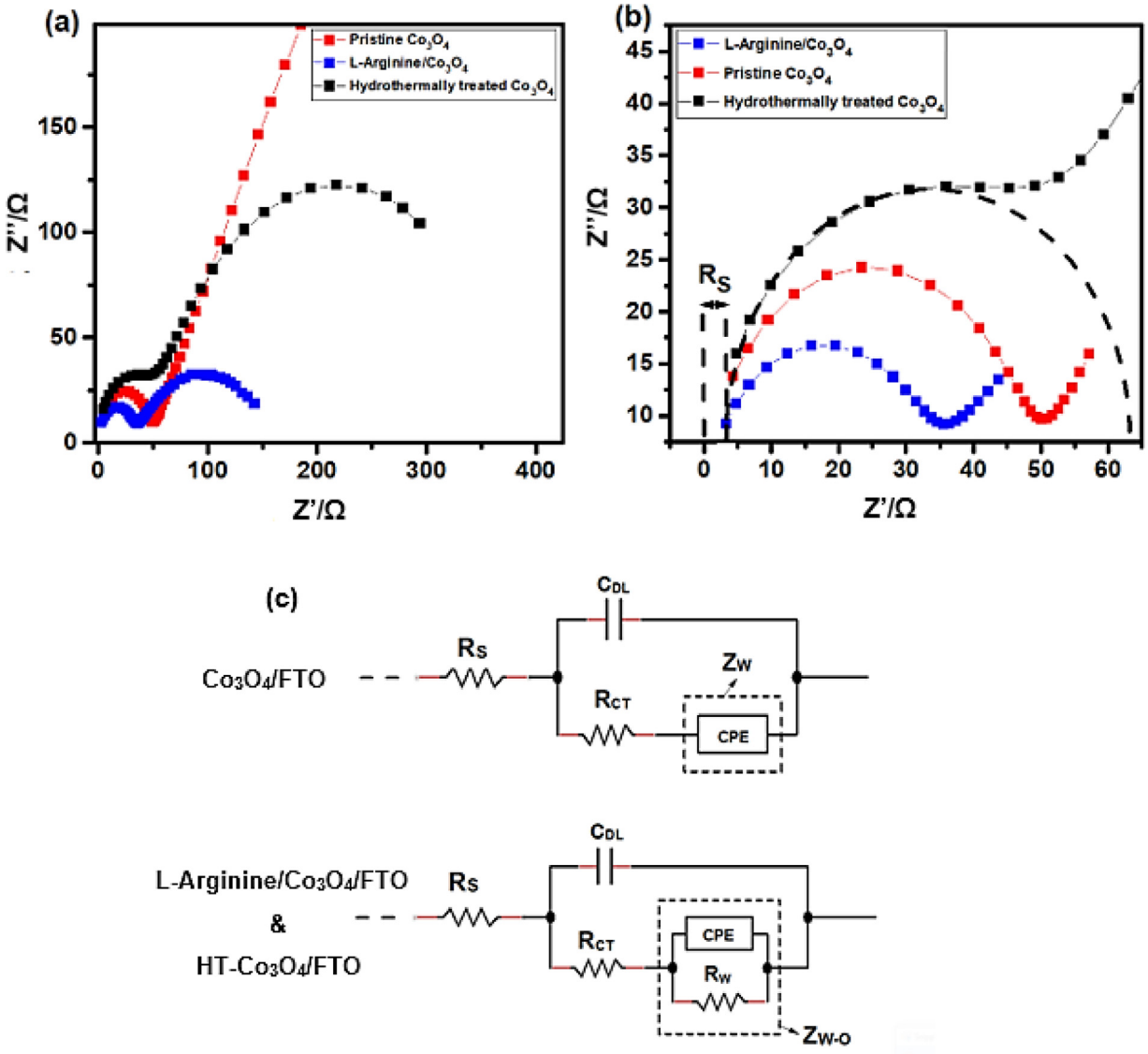

Fig. 8. a) Nyquist plots for Co_3O_4/FTO, HT-Co_3O_4/FTO, and L-Arginine/Co_3O_4/FTO in 0.1 M KCl + 5 mM $K_3[Fe(CN)_6]$; b) The high frequency region of the Nyquist plots and c) Randles equivalent circuits.

plot is fitted with Randles equivalent circuits as shown in Fig. 8c, where R_S is the solution resistance, R_{CT} is the charge transfer resistance, C_{DL} is the double layer capacitance, CPE is the constant phase arising from surface inhomogeneity [77], R_W is the Warburg diffusion resistance, Z_W is the semi-infinite Warburg impedance, and $Z_{W\text{-}O}$ is the finite-length Warburg impedance, represented here by the parallel arrangement of CPE and R_W [78]. The CPE exponent (n) for HT-Co_3O_4/FTO, Co_3O_4/FTO, and L-Arginine/Co_3O_4/FTO was found to be 0.79, 0.62, and 0.59, respectively (Table S4 in supporting documentation). This decreasing trend can be related to an increase in electrode roughness. This was also observed from SEM images. It can be seen from Fig. 8b that the L-Arginine/Co_3O_4/FTO (R_{CT} = 32.4 Ω) has a smaller charge transfer resistance than compared to Co_3O_4/FTO (R_{CT} = 47.7 Ω) and HT-Co_3O_4/FTO (R_{CT} = 59.2 Ω) electrodes. The smaller charge transfer resistance for L-Arginine/Co_3O_4/FTO compared with Co_3O_4/FTO and HT-Co_3O_4/FTO is certainly promoted by positively charged functional groups creating more ionic pathways. Moreover, the semicircles in Fig. 8b show a decreasing trend in the double layer capacitances (values retrieved from EIS data) of the three electrodes, from L-Arginine/Co_3O_4/FTO (C_{DL}= 0.156 μF) through Co_3O_4/FTO (C_{DL}= 0.105 μF) to HT-Co_3O_4/FTO (C_{DL}= 0.091 μF). Normalizing the double layer capacitance by specific capacitance of a smooth planar electrode (assumed C_S = 40 μF/cm^2) gives the electrochemical active surface area (ECSA) [79]. The ECSA were found to be 0.0039, 0.00263 and 0.00228 cm^2 for L-Arginine/Co_3O_4/FTO, Co_3O_4/FTO and HT-Co_3O_4/FTO, respectively. The higher ECSA for L-Arginine/Co_3O_4/FTO resulted in enhanced electrocatalytic activity compared with the other electrodes studied. Tafel plot was further utilized to support the EIS results, as seen in Figure S4 (electronic supplementary document). It was found that the Tafel slope (i.e., overpotential) for L-Arginine/Co_3O_4/FTO (110 mV) is smaller than those for Co_3O_4/FTO (116 mV) and HT-Co_3O_4/FTO (235 mV) due to reduced charge transfer resistance. Table S4 presents measured and calculated electrochemical parameters for the prepared electrodes.

3.2.3. Nitrite sensing mechanism

Based on physical and electrochemical characterizations, it is evident that the low oxidation states of cobalt (Co^0 and Co^{2+}) behave as redox-active sites for the electrooxidation of nitrite in neutral environment. The occurrence of nitrite oxidation at Co(II) rather than Co(III) in aqueous media can be due to a stabilization

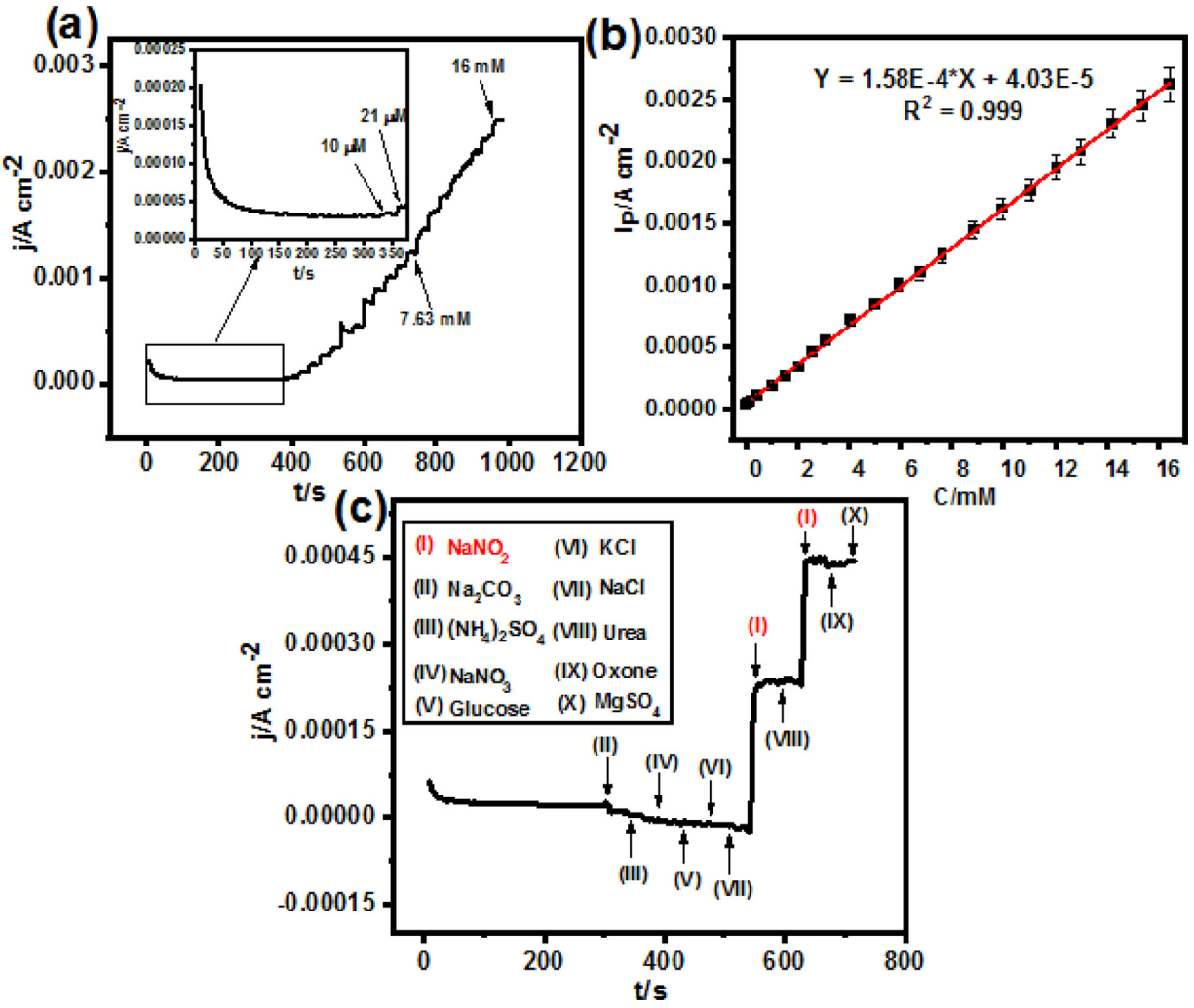

Fig. 9. a) Chronoamperometry data for L-Arginine/Co_3O_4/FTO in 0.1 M PBS (pH = 7.4), (b) Dose response curve of the as prepared electrode, and (c) Interference study of L-Arginine/Co_3O_4/FTO for nitrite in 0.1 M PBS and in the presence of Na_2CO_3, $(NH_4)_2SO_4$, Na_2NO_3, glucose, KCl, NaCl, urea, oxone, and $MgSO_4$.

effect of nitrite on Co(III). Nitrite (N-bonded) as a strong field ligand [80] can stabilize Co(III) (low spin), decreasing by that means the reducing tendency and oxidizing power of Co(III), and resulting into the preferential interaction of nitrite with Co(II) [81]. The following reaction mechanism is proposed for the interaction of nitrite at L-Arginine/Co_3O_4/FTO:

a) The metallic phase of cobalt (Co^0) has additive effect on the amount of divalent cobalt (Co^{2+}) in solution (Equation 8);
b) The reaction proceeds via the formation of an adduct between cobalt oxide and nitrite through the divalent cobalt (Co^{2+}) (Equation 9);
c) A slow, one-electron transfer process involving the simultaneous oxidation of Co^{2+} and NO_2^- to Co^{3+} and NO_2, occurs (Equation 10). This is evidenced by the CV experiment in Fig. 8b for L-Arginine/Co_3O_4/FTO;
d) Finally, NO_2 undergoes disproportionation Equation 11-(12) and Co^{3+} is reduced to Co^{2+} (Equation 13).

$$(Co^0Co^{2+})(L-\text{Arginine}/Co_3O_4/\text{FTO})+H_2O \rightarrow Co^{2+}(L-\text{Arginine}/Co_3O_4/\text{FTO})+2e^- \quad (8)$$

$$Co^{2+}(L-\text{Arginine}/Co_3O_4/\text{FTO})+NO_2^- \leftrightarrow Co^{2+}\left(NO_2^-\right)(L-\text{Arginine}/Co_3O_4/\text{FTO}) \quad (9)$$

$$\left[Co^{2+}\left(NO_2^-\right)(L-\text{Arginine}/Co_3O_4/\text{FTO})\right] \leftrightarrow Co^{3+}(L-\text{Arginine}/Co_3O_4/\text{FTO})+NO_2 \quad (10)$$

$$2NO_2+H_2O \leftrightarrow 2H^++NO_3^-+NO_2^- \quad (11)$$

$$NO_2^-+H_2O \rightarrow 2H^++NO_3^-+2e^- \quad (12)$$

$$Co^{3+}(L-\text{Arginine}/Co_3O_4/\text{FTO}) \rightarrow Co^{2+}(L-\text{Arginine}/Co_3O_4/\text{FTO})+e^- \quad (13)$$

3.3. Chronoamperometric study of the as prepared electrode

Chronoamperometry measurements (Fig. 9a) were conducted in the presence of successive injection of nitrite under mild stirred condition and at a fixed potential of 0.96 V vs Ag/AgCl. The sensor exhibited a sensitivity of 158 μA/mM cm^{-2} and linear range of up to 16 mM (Fig. 9b). An ultra-fast steady state response time of < 2 s was also observed. The limit of detection (LOD) was calculated using the formula $3\sigma/S$ [82], with σ, being the standard deviation of the response (estimated by the standard deviation of y-intercepts) [83] and S, is the sensitivity. The calculated LOD (1.95 nM) is significantly lower than the maximum allowable nitrite concentration in drinking water (65 μM) in accordance with WHO. This qualifies the fabricated sensor for practical applications, including nitrite detection in drinking water. The obtained sensor

Table 1
Comparison of performance characteristics of the developed electrochemical nitrite sensors with the reported sensors in literature.

Modified Electrode	Technique	Electrolyte	pH	E/mV	C/μM	S/μA mM^{-1}	LOD/μM	Reference
[a](FeT4MPyP + CoTSPc)/GCE	Amperometry	PBS	7	850 vs SCE	0.2 - 8.6	0.37	0.04	[85]
[b]Co_3O_4/RGO/GCE	Amperometry	KOH	14	-	1 - 380	2065	0.14	[86]
[c]CoTBMPc-Au	CV	PBS	7.4	750 vs Ag/AgCl	100 - 1000	7.3×10^{-3}	-	[87]
[d]CoTDMPc-Au	CV	PBS	7.4	770 vs Ag/AgCl	100 - 1000	7.1×10^{-3}	-	[87]
[e]CoO_x/CNT/GCE	Amperometry	PBS	6.76	750 vs SCE	0.5 - 249	5.619×10^{-2}	0.3	[88]
[f]polyNiCo/GCE	Amperometry	PBS	7	-	2.49 - 1700	0.027	0.45	[74]
	CV	PBS	7	850 vs Ag/AgCl	100 - 5000	0.042	10	
[g]Co_3O_4-DCS/GCE	Amperometry	PBS	7	900 vs SCE	6.6 - 300	0.318	0.22	[71]
					300 - 13480	0.6		
[h]Pt/CoO/GCE	Amperometry	PBS	6	900 vs SCE	0.2 - 3670	0.9014	0.067	[89]
					3670 - 23700	0.4085		
[i]NC/GCE	Amperometry	PBS	7	900 vs SCE	5 - 4000	1.21×10^{-4}	0.002	[90]
[j](CoTsPc/PDDA-Gr) $_n$/GCE	Amperometry	PBS	5	800 vs SCE	2 - 36	5.3×10^{-3}	0.084	[91]
[k]EPPGE-SWCNT-Co	CV	PBS	7.4	900 vs Ag/AgCl	0 - 189	0.2496	5.61	[92]
[L]CoPc/MWCNTs/GCE	DPV	PBS	7.4	972 vs Ag/AgCl	10 - 1050000	4×10^{-5}	2.11	[93]
[m]CoPcF-MWCNTs/GCE	Amperometry	PBS	7	800 vs SCE	0.096 - 340	0.0299	0.062	[94]
[n]Co_3O_4-rGO/CNTs/GCE	Amperometry	PBS	7	800 vs Ag/AgCl	0.1 - 8000	0.08	0.016	[82]
Co@Pt/Gr	Amperometry	PBS	6	850 vs Ag/AgCl	1 - 2000	4.596×10^{-2}	0.145	[95]
					2000 - 15000	9.771×10^{-2}		
[p]CoNS/GO/PPy/GCE	CV	PBS	8	800 vs SCE	1 - 3167	0.5192	0.0147	[96]
[q]CoTM-QOPc/CNP/GCE	CV	PBS	7	790 vs Ag/AgCl	0.2–200	2.3	0.06	[97]
	DPV	PBS	7	740 vs Ag/AgCl	0.2–225	1.03	0.06	
	Amperometry	PBS	7	740 vs Ag/AgCl	0.1–350	1.24	0.033	
[r]CuO-NS/GCE	DPV	PBS	7	850 vs SCE	100-1400	6.17×10^{-3}	13.6	[98]
[s](HOOC-MWCNT)/GCE	DPV	PBS	7	720 vs SCE	100-700	0.2099	0.565	[99]
[t]L-Arginine/Co_3O_4/FTO	Amperometry	PBS	7.4	960 vs Ag/AgCl	10 - 16000	158	0.00195	This work

[a] (FeT4MPyP + CoTSPc)/GCE: glassy carbon electrode modified with alternated layers of iron(III) tetra-(N-methyl-4-pyridyl)-porphyrin and cobalt(II) tetrasulfonated phthalocyanine. [b]Co_3O_4/RGO/GCE: cobalt oxide nanospindles-decorated reduced graphene oxide composite on GCE. [c]CoTBMPc-Au & [d]CoTDMPc-Au: Co(II) tetrakis (benzylmercapto) and tetrakis (dodecylmercapto) phthalocyanines electrodeposited onto a gold electrode. [e]CoO_x/CNT/GCE: cobalt oxide nanoparticles on multi-walled carbon nanotubes deposited on a conventional GCE.

[f] polyNiCo/GCE: Ni(II) and Co(II)- bisterpyridine ligand based heterometallo SMP. [g]Co_3O_4-DCS/GCE: glassy carbon electrode modified with cobalt oxide disordered circular sheet. [h]Pt/CoO/GCE: platinum nanoclusters doped CoO nanohybrid on GCE. [i]NC/GCE: urchin-like nickel-cobalt carbonate hollow spheres on GCE. [j](CoTsPc/PDDA-Gr)$_n$/GCE: graphene/cobalt phthalocyanine composite film on activated GCE. [k]EPPGE-SWCNT-Co: edge plane pyrolytic graphite electrode (with cobalt nanoparticles integrated with single-walled carbon nanotubes. [L]CoPc/MWCNTs/GCE: GCE modififed with cobalt (II) phthalocyanine immobilized on multiwalled carbon nanotubes. [m]CoPcF-MWCNTs/GCE: cobalt phthalocyanine functionalized multiwalled carbon nanotubes on GCE. [n]Co_3O_4-rGO/CNTs/GCE: cobalt oxide decorated reduced graphene oxide and carbon nanotubes on GCE. °: cobalt @ platinum nanoparticles-decorated graphene. [p]CoNS/GO/PPy/GCE: cobalt nanostructures, graphene oxide-doped polypyrrole modified GCE. [q]CoTM-QOPc/CNP/GCE: cobalt (II) tetra methyl-quinoline oxy bridged phthalocyanine carbon nano particles modified glassy carbon electrode. [r]CuO-NS/GCE: Copper oxide nanosheet modified GCE. [s](HOOC-MWCNT)/GCE: Acid-functionalized multi-walled carbon nanotubes modified GCE. [t]L-Arginine/Co_3O_4/FTO: L-Arginine modified cobalt oxide thin film on FTO.

performance characteristics were compared with literature, as reported in Table 1. Most of the sensor data presented in the literature uses a glassy carbon as substrate. This approach is not commercially viable. Moreover, the as prepared sensor reported in this study showed a combination of ultra-low limit of detection, ultrafast response time, high sensitivity & selectivity and wide linear range. Such electrochemical nitrite sensor performance characteristics combination is rare in the reported literature. This makes the developed sensor a potential candidate for commercial application.

The selectivity of L-Arginine/Co_3O_4/FTO towards nitrite oxidation was evaluated in the presence of interfering species that may coalesce with nitrite during its detection. A five times higher concentration than that of nitrite was used in 0.1 M PBS solution for each of the following interfering substances: Na_2CO_3, $(NH_4)_2SO_4$, $NaNO_3$, glucose, KCl, NaCl, urea, oxone, and $MgSO_4$. As prepared L-Arginine/Co_3O_4/FTO sensor was only responsive to nitrite injection and the presence of interferants did not reduce the sensor response, as seen in Fig. 9c. It is more likely that the interfering cations (Na^+, NH_4^+, K^+, and Mg^{2+}) will experience charge repulsion due to positively charged functional groups immobilized on L-Arginine/Co_3O_4/FTO. Also, the enrichment of neutral organic compounds like glucose and urea on the surface of L-Arginine/Co_3O_4/FTO can be prevented because of the competition with anionic species. The excellent selectivity of L-Arginine/Co_3O_4/FTO towards nitrite compared with the other anions investigated agrees largely with the Hofmeister series [84], except for nitrate which deviated from Hofmeister pattern. Another possible explanation for the good selectivity could be the interfering anions (CO_3^{2-}, SO_4^{2-}, HSO_5^-, HSO_4^-, NO_3^-, and Cl^-) as weak-field ligands interact weakly with the divalent cobalt on L-Arginine/Co_3O_4/FTO in aqueous solution. Nitrite (N-bonded), on the contrary, is a stronger field ligand and gives rise to bigger coordination forces.

3.3.1. Electrochemical stability and reproducibility study of the as prepared electrode

Cyclic voltammetry (CV) and chronoamperometry were used to study the stability and reproducibility of the L-Arginine/Co_3O_4/FTO sensor. The electrochemical stability test is shown in Fig. 10a. The absence of any additional peaks after 25th cycle highlights the electrochemical stability of the as prepared sensor. For reproducibility, five independent electrodes were tested using CV and individual current responses were compared as depicted in the histogram presented in Fig. 10b. A relative standard deviation (% RSD) of 1.52 % was obtained. This highlights the excellent reproducibility of L-Arginine/Co_3O_4/FTO electrode. In addition, long-term chronoamperometric study (Fig. 10c) revealed that oxidation current response decreased only by 12 % over a period of 19 min.

3.3.2. Detection of nitrite in real sample

The real sample test was carried following the protocol described in [100]. The recovery study in tap water sample was conducted to investigate the practical application of L-Arginine/Co_3O_4/FTO electrode for nitrite detection. For this reason, tap water samples were diluted with 0.1 M PBS solution (pH = 7.4)

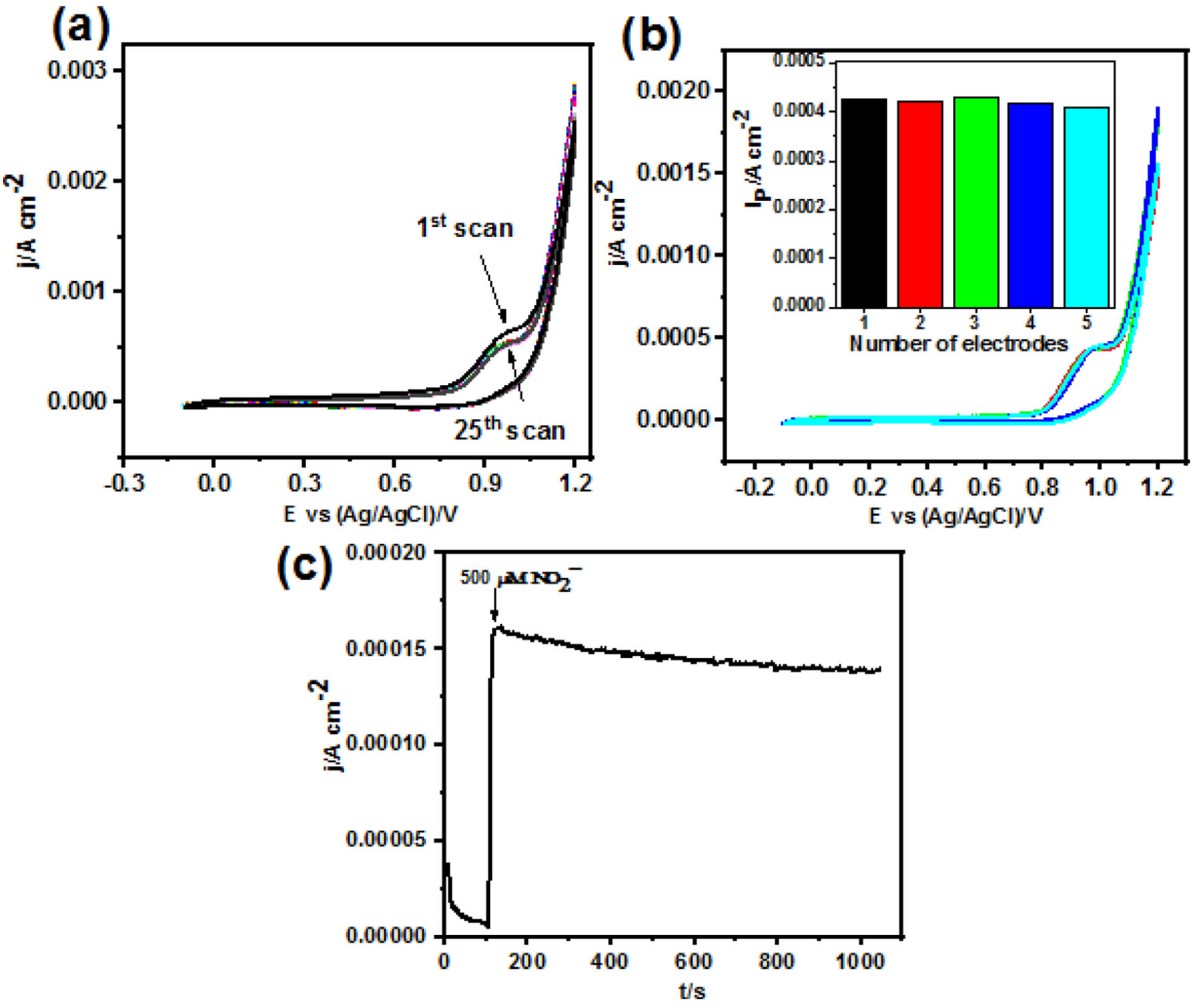

Fig. 10. a) Stability study of L-Arginine/Co_3O_4/FTO in the presence of 2 mM nitrite in 0.1 M PBS at 10 mVs^{-1} for 25 scans; b) Reproducibility test of five different L-Arginine/Co_3O_4/FTO electrodes in the presence of 2 mM nitrite in 0.1 M PBS at 10 mVs^{-1} and c) Long-term chronoamperometry of L-Arginine/Co_3O_4/FTO in the presence of 500 µM nitrite in in 0.1 M PBS over 19 min.

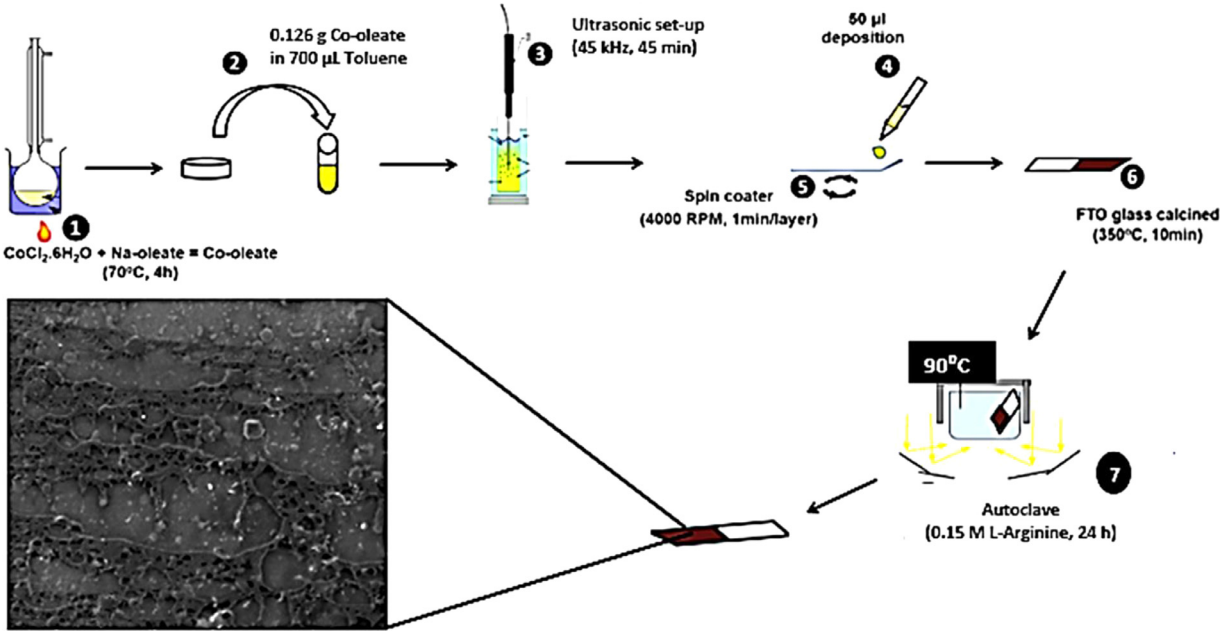

Scheme 1. Schematic illustration for the fabrication of L-Arginine modified Co_3O_4 thin film for nitrite detection.

Table 2
Recovery study of nitrite ions in tap water.

Sample	Spiked (mM)	Found (mM)	Recovery (%)
Tap water	0.60	0.61	101,7
	1.40	1.41	100.7
	1.50	1.54	102.7
	1.70	1.66	97.6
	2.50	2.42	96.8

and tested for nitrite ions. The test results are summarized in Table 2. It can be seen from Table 2 that the sensor shows good recovery rates ranging from 96.8 % to 101.7 %, with an average value of 99.9 %.

4. Conclusions

In summary, we have successfully ($CH_6N_3^+$, NH_3^+)-functionalized and nitrogen doped Co_3O_4 by hydrothermal treatment of Co_3O_4 in the presence of L-Arginine. Spectral evidence is presented on how hydrothermal treatment can reduce oxygen vacancy and how nitrogen atoms can compete for substitution into Co_3O_4 crystal lattice. This technique can serve as a new platform for post deposition element doping and surface functionalization of metal oxides for various sensing applications. The L-Arginine treated electrode exhibited enhanced electrochemical nitrite detection compared to pristine Co_3O_4 electrode. The enhanced electrochemical performance originated from: 1) the faster electron transport kinetics, which is a result of nitrogen doping and surface functional groups (i.e., $CH_6N_3^+$ and NH_3^+), 2) the availability of higher ECSA (increased amount of Co^0 and Co^{2+} as active sites due to N doping), and 3) the easy access to active sites and better mass transport kinetics promoted by the porous surface of L-Arginine/Co_3O_4/FTO.

Author statement

Ariel Ndala[1]: Original draft preparation, editing, methodology, data Collection, data interpretation; **Bamato Itota & Christopher Sunday**: Data curation; **Jessica chamier & Sekhar Ray**: Data collection, editing; **Mahabubur Chowdhury*:** Editing, original Idea, grant, and supervision.

Electronic Supplementary Document revised_ndala_chowdhury.docx

Figure S1: XRD patterns of the MOD derived Co_3O_4 Electrode
Table S1. Surface atomic compositions [%]
Figure S2: a) C 1*s* XPS spectrum for Co_3O_4/FTO, HT-Co_3O_4/FTO, and L-Arginine/Co_3O_4/FTO thin films; deconvolution of C1s XPS spectra for b) Co_3O_4/FTO, c) L-Arginine/Co_3O_4/FTO, and d) HT-Co_3O_4/FTO.
Figure S3: a) O 1*s* XPS spectral lines for Co_3O_4/FTO, HT-Co_3O_4/FTO, and L-Arginine/Co_3O_4/FTO thin films; deconvoluted O1s XPS peaks for b) Co_3O_4/FTO, c) L-Arginine/Co_3O_4/FTO, and d) HT-Co_3O_4/FTO.
Table S2. Summary of binding energy peak positions for Co $2p_{3/2}$ XPS deconvolution for Co_3O_4/FTO, HT-Co_3O_4/FTO, and L-Arginine/Co_3O_4/FTO
Figure S4: Tafel plots of the L-Arginine/Co_3O_4/FTO, HT-Co_3O_4/FTO, and Co_3O_4/FTO electrodes.
Table S4. Measured and calculated electrochemical parameters for L-Arginine/Co_3O_4/FTO, Co_3O_4/FTO, and HT-Co_3O_4/FTO. Tafel slope, k^0, [R_{CT}, C_{DL}, R_W, and n], and ECSA were obtained from (1) Tafel plot in Figure S4, (2) Equation 7 in the manuscript, (3) EIS data using Randles equivalent circuit, and (4) the division of C_{DL} values by specific capacitance ($C_S = 40\ \mu F/cm^2$), respectively.

Declaration of Competing Interest

The authors declare that they have no known competing financial interests or personal relationships that could have appeared to influence the work reported in this paper.

Acknowledgments

Mahabubur Chowdhury would like to thank the National Research Foundation of South Africa for financial support (TTK180417322190).

References

[1] A. Wachter, Sodium nitrite as corrosion inhibitor for water, Ind. Eng. Chem. 37 (8) (1945) 749–751, doi:10.1021/ie50428a021.
[2] S. Hosoya, Sulfuric acid bleaching of kraft pulp II: Behavior of lignin and carbohydrate during sulfuric acid bleaching, J. Wood Sci. 45 (4) (1999) 313–318, doi:10.1007/bf00833496.
[3] K.O. Honikel, The use and control of nitrate and nitrite for the processing of meat products, Meat Sci 78 (1–2) (2008) 68–76, doi:10.1016/j.meatsci.2007.05.030.
[4] H. Kroupova, J. Machova, Z. Svobodova, Nitrite influence on fish: a review, Vet. Med. (Praha). 50 (11) (2005) 461–471, doi:10.17221/5650-VETMED.
[5] J.D. Brender, J.M. Olive, M. Felkner, L. Suarez, W. Marckwardt, K.A. Hendricks, Dietary nitrites and nitrates, nitrosatable drugs, and neural tube defects, Epidemiology 15 (3) (2004) 330–336, doi:10.1097/01.ede.0000121381.79831.7b.
[6] Y. Sayato, WHO guidelines for drinking-water quality, Eisei kagaku 35 (5) (1989) 307–312, doi:10.1248/jhs1956.35.307.
[7] H. Li, C.J. Meininger, G. Wu, Rapid determination of nitrite by reversed-phase high-performance liquid chromatography with fluorescence detection, J. Chromatogr. B Biomed. Sci. Appl. 746 (2) (2000) 199–207, doi:10.1016/S0378-4347(00)00328-5.
[8] A.T. Mubarak, A.A. Mohamed, K.F. Fawy, A.S. Al-Shihry, A novel kinetic determination of nitrite based on the perphenazine-bromate redox reaction, Microchim. Acta 157 (1–2) (2007) 99–105, doi:10.1007/s00604-006-0661-3.
[9] D. He, Z. Zhang, Y. Huang, Y. Hu, Chemiluminescence microflow injection analysis system on a chip for the determination of nitrite in food, Food Chem 101 (2) (2007) 667–672, doi:10.1016/j.foodchem.2006.02.024.
[10] F. Wang, S. Hu, Electrochemical sensors based on metal and semiconductor nanoparticles, Microchim. Acta 165 (2009) 1–2 1–22, doi:10.1007/s00604-009-0136-4.
[11] L.M. Rossi, N.J.S. Costa, F.P. Silva, R. Wojcieszak, Magnetic nanomaterials in catalysis: advanced catalysts for magnetic separation and beyond, Green Chem 16 (6) (2014) 2906–2933, doi:10.1039/c4gc00164h.
[12] V.E. Bochenkov, G.B. Sergeev, Nanomaterials for sensors, Russ. Chem. Rev. 76 (11) (2007) 1084–1093, doi:10.1070/rc2007v076n11abeh003735.
[13] L.H. Chen, J.B. Zang, Y.H. Wang, L.Y. Bian, Electrochemical oxidation of nitrite on nanodiamond powder electrode, Electrochim. Acta 53 (8) (2008) 3442–3445, doi:10.1016/j.electacta.2007.12.023.
[14] Y. Astier, G.W. Canters, J.J. Davis, H.A.O. Hill, M.P. Verbeet, H.J. Wijma, Sensing nitrite through a pseudoazurin-nitrite reductase electron transfer relay, ChemPhysChem 6 (6) (2005) 1114–1120, doi:10.1002/cphc.200400384.
[15] Y. Cui, C. Yang, W. Zeng, M. Oyama, W. Pu, J. Zhang, Electrochemical determination of nitrite using a gold nanoparticles- modified glassy carbon electrode prepared by the seed-mediated growth technique, Anal. Sci. 23 (12) (2007) 1421–1425, doi:10.2116/analsci.23.1421.
[16] Y. Ma, In situ growth of α-Fe_2O_3 nanorod arrays on 3D carbon foam as an efficient binder-free electrode for highly sensitive and specific determination of nitrite, J. Mater. Chem. A 5 (9) (2017) 4726–4736, doi:10.1039/c6ta10744c.
[17] M. Lamine, Toxicity and Electrochemical Detection of Lead, Cadmium and Nitrite Ions by Organic Conducting Polymers : A Review, Chem. Africa (0123456789) (2020), doi:10.1007/s42250-020-00157-0.
[18] Y. Gangarajula, B. Gopal, Spinel cobalt oxide catalyzed controlled hydration of aromatic nitriles, Chem. Lett. 41 (1) (2012) 101–103, doi:10.1246/cl.2012.101.
[19] R. Xu, Porous cobalt oxide (Co_3O_4) nanorods: Facile syntheses, optical property and application in lithium-ion batteries, J. Solid State Chem. 182 (11) (2009) 3177–3182, doi:10.1016/j.jssc.2009.08.033.
[20] A.M. Cao, Hierarchically structured cobalt oxide (Co_3O_4): The morphology control and its potential in sensors, J. Phys. Chem. B 110 (32) (2006) 15858–15863, doi:10.1021/jp0632438.
[21] W.L. Roth, The magnetic structure of Co_3O_4,", J. Phys. Chem. Solids 25 (1) (1964) 1–10, doi:10.1016/0022-3697(64)90156-8.
[22] Y. Hou, Enhancing the electrocatalytic activity of 2D micro-assembly Co_3O_4 nanosheets for Li–O_2 batteries by tuning oxygen vacancies and Co^{3+}/Co^{2+} ratio, Electrochim. Acta 324 (2019) 134884, doi:10.1016/j.electacta.2019.134884.
[23] Z. Zhu, G. Lu, Z. Zhang, Y. Guo, Y. Guo, Y. Wang, Highly active and stable Co_3O_4/ZSM-5 catalyst for propane oxidation: Effect of the preparation method, ACS Catal 3 (6) (2013) 1154–1164, doi:10.1021/cs400068v.
[24] K. Nakaoka, M. Nakayama, K. Ogura, Electrochemical Deposition of Spinel-Type Cobalt Oxide from Alkaline Solution of Co[sup 2+] with Glycine, J. Electrochem. Soc. 149 (3) (2002) C159, doi:10.1149/1.1446871.

[25] B. Han, K.H. Choi, K. Park, W.S. Han, W.J. Lee, Low-temperature atomic layer deposition of cobalt oxide thin films using dicobalt hexacarbonyl tert-butylacetylene and ozone, Electrochem. Solid-State Lett. 15 (2) (2012) 2012–2015, doi:10.1149/2.008202esl.

[26] L.C. Schumacher, I.B. Holzhueter, I.R. Hill, M.J. Dignam, Semiconducting and electrocatalytic properties of sputtered cobalt oxide films, Electrochim. Acta 35 (6) (1990) 975–984, doi:10.1016/0013-4686(90)90030-4.

[27] H.S. Jeon, M.S. Jee, H. Kim, S.J. Ahn, Y.J. Hwang, B.K. Min, Simple Chemical Solution Deposition of Co_3O_4 Thin Film Electrocatalyst for Oxygen Evolution Reaction, ACS Appl. Mater. Interfaces 7 (44) (2015) 24550–24555, doi:10.1021/acsami.5b06189.

[28] M. Biswas, P.-C. Su, Chemical Solution Deposition Technique of Thin-Film Ceramic Electrolytes for Solid Oxide Fuel Cells, Mod. Technol. Creat. Thin-film Syst. Coatings (2017) May,, doi:10.5772/66125.

[29] R.W. Schwartz, Chemical Solution Deposition of Perovskite Thin Films, Chem. Mater. 9 (11) (1997) 2325–2340, doi:10.1021/cm970286f.

[30] M. Chowdhury, C. Ossinga, F. Cummings, J. Chamier, M. Kebede, Novel Sn Doped Co_3O_4 Thin Film for Nonenzymatic Glucose Bio-Sensor and Fuel Cell, Electroanalysis 29 (8) (2017) 1876–1886, doi:10.1002/elan.201700184.

[31] M. Palmer, Enhanced electrochemical glucose sensing performance of CuO:NiO mixed oxides thin film by plasma assisted nitrogen doping, J. Alloys Compd. 853 (2021) 156900, doi:10.1016/j.jallcom.2020.156900.

[32] F. Hua, M.T. Swihart, E. Ruckenstein, Efficient surface grafting of luminescent silicon quantum dots by photoinitiated hydrosilylation, Langmuir 21 (13) (2005) 6054–6062, doi:10.1021/la0509394.

[33] D. Patel, Y. Chang, G.H. Lee, Amino acid functionalized magnetite nanoparticles in saline solution, Curr. Appl. Phys. 9 (1 SUPPL.) (2009) S32–S34, doi:10.1016/j.cap.2008.08.027.

[34] C. Lewis, Effect of pH on the Binding of Sodium, Lysine, and Arginine Counterions to l-Undecyl Leucinate Micelles, J. Surfactants Deterg. 19 (6) (2016) 1175–1188, doi:10.1007/s11743-016-1875-y.

[35] R.J.T. Houk, S.L. Tobey, E.V. Anslyn, Abiotic guanidinium receptors for anion molecular recognition and sensing, Top. Curr. Chem. 255 (2005) 199–229, doi:10.1007/b101167.

[36] D.H. Kim, The role of arginine as nitrogen doping and carbon source for enhanced oxygen reduction reaction, Int. J. Hydrogen Energy 43 (3) (2018) 1479–1488, doi:10.1016/j.ijhydene.2017.11.173.

[37] M. Li, Air stable and reversible n-type surface functionalization of MoS_2 monolayer using Arg and Lys amino acids, J. Mater. Chem. C (2020), doi:10.1039/d0tc02939d.

[38] D.K. Bora, A. Braun, R. Erni, G. Fortunato, T. Graule, E.C. Constable, Hydrothermal treatment of a hematite film leads to highly oriented faceted nanostructures with enhanced photocurrents, Chem. Mater. 23 (8) (2011) 2051–2061, doi:10.1021/cm102826n.

[39] H. Cao, G. Wang, J.H. Warner, A.A.R. Watt, Amino-acid-assisted synthesis and size-dependent magnetic behaviors of hematite nanocubes, Appl. Phys. Lett. 92 (1) (2008) 1–4, doi:10.1063/1.2830699.

[40] M. Harry, M. Chowdhury, F. Cummings, C.J. Arendse, Elemental Cu doped Co_3O_4 thin film for highly sensitive non-enzymatic glucose detection, Sens. Bio-Sensing Res. 23 (2019) 100262 Apr., doi:10.1016/J.SBSR.2019.100262.

[41] M. Chowdhury, F. Cummings, M. Kebede, V. Fester, Binderless Solution Processed Zn Doped Co_3O_4 Film on FTO for Rapid and Selective Non-enzymatic Glucose Detection, Electroanalysis 29 (2) (2017) 578–586, doi:10.1002/elan.201600440.

[42] J.J. Wang, Y. Hu, R. Toth, G. Fortunato, A. Braun, A facile nonpolar organic solution process of a nanostructured hematite photoanode with high efficiency and stability for water splitting, J. Mater. Chem. A 4 (8) (2016) 2821–2825, doi:10.1039/c5ta06439b.

[43] A. Diallo, A.C. Beye, T.B. Doyle, E. Park, M. Maaza, Green synthesis of Co_3O_4 nanoparticles via Aspalathus linearis: Physical properties, Green Chem. Lett. Rev. 8 (3–4) (2015) 30–36, doi:10.1080/17518253.2015.1082646.

[44] B. De Rivas, R. López-Fonseca, C. Jiménez-González, J.I. Gutiérrez-Ortiz, Synthesis, characterisation and catalytic performance of nanocrystalline Co_3O_4 for gas-phase chlorinated VOC abatement, J. Catal. 281 (1) (2011) 88–97, doi:10.1016/j.jcat.2011.04.005.

[45] C. Ouyang, X. Wang, S. Wang, Phosphorus-doped CoS2 nanosheet arrays as ultra-efficient electrocatalysts for the hydrogen evolution reaction, Chem. Commun. 51 (75) (2015) 14160–14163, doi:10.1039/c5cc05541e.

[46] Q. Hao, S.M. Morton, B. Wang, Y. Zhao, L. Jensen, T.Jun Huang, Tuning surface-enhanced Raman scattering from graphene substrates using the electric field effect and chemical doping, Appl. Phys. Lett. 102 (1) (2013), doi:10.1063/1.4755756.

[47] G. Socrates, Infrared and Raman characteristic group frequencies. Tables and charts, 2001 Third.

[48] P. Larkin, IR and Raman Spectra-Structure Correlations: Characteristic Group Frequencies, in: P. Larkin (Ed.), IR and Raman Spectroscopy Principles and Spectral Interpretation, Elsevier, 2011, pp. 73–115.

[49] B.A. Kolesov, Raman spectra of single H_2O molecules isolated in cavities of crystals, J. Struct. Chem. 47 (1) (2006) 21–34, doi:10.1007/s10947-006-0261-4.

[50] S. Kumar, S.B. Rai, Spectroscopic studies of L-arginine molecule, Indian J. Pure Appl. Phys. 48 (4) (2010) 251–255.

[51] P.T.C. Freire, F.M. Barboza, J.A. Lima, F.E.A. Melo, J.M. Filho, Raman Spectroscopy of Amino Acid Crystals, Raman Spectrosc. Appl. (2017), doi:10.5772/65480.

[52] G. Zhu, X. Zhu, Q. Fan, X. Wan, Raman spectra of amino acids and their aqueous solutions, Spectrochim. Acta - Part A Mol. Biomol. Spectrosc. 78 (3) (2011) 1187–1195, doi:10.1016/j.saa.2010.12.079.

[53] Y. Zheng, Y. Liu, H. Zhou, W. Huang, Z. Pu, Complete combustion of methane over Co_3O_4 catalysts: Influence of pH values, J. Alloys Compd. (2017), doi:10.1016/j.jallcom.2017.11.008.

[54] R. Finkler, L.T. Coutrim, P.G. Pagliuso, F. Stavale, E.M. Bittar, in: Training-induced inversion of spontaneous exchange bias field on $La_{1.5}Ca_{0.5}CoMnO_6$, 2018, pp. 1–9.

[55] Y. Zheng, Y. Yu, H. Zhou, W. Huang, Z. Pu, Combustion of lean methane over Co_3O_4 catalysts prepared with different cobalt precursors, RSC Adv 10 (8) (2020) 4490–4498, doi:10.1039/c9ra09544f.

[56] X. Sun, Spectroscopic study of Zn2+ and Co2+ binding to extracellular polymeric substances (EPS) from aerobic granules, J. Colloid Interface Sci. 335 (1) (2009) 11–17, doi:10.1016/j.jcis.2009.03.088.

[57] S. Zhan, H. Zhang, X. Mi, Y. Zhao, C. Hu, and L. Lyu, "Treatment and Resource Recovery Efficient Fenton-like Process for Pollutant Removal in Electron-Rich /Poor Reaction Sites Induced by Surface Oxygen Vacancy over Cobalt-Zinc Oxides Key Laboratory of Pollution Processes and Environmental Criteria Tianjin K," 2020, doi: 10.1021/acs.est.9b07245.

[58] A. Amri, X. Duan, C. Yin, Z. Jiang, M.M. Rahman, T. Pryor, Applied Surface Science Solar absorptance of copper – cobalt oxide thin film coatings with nano-size, grain-like morphology : Optimization and synchrotron radiation XPS studies, Appl. Surf. Sci. 275 (2013) 127–135, doi:10.1016/j.apsusc.2013.01.081.

[59] H. Pan, Microwave-Assisted Synthesis of Co/CoO_x Supported on Earth-Abundant Coal-Derived Carbon for Electrocatalysis of Oxygen Evolution Microwave-Assisted Synthesis of Co/CoO_x Supported on Earth-Abundant Coal-Derived Carbon for Electrocatalysis of Oxygen *et al.*, 2019, doi:10.1149/2.0281908jes.

[60] S. Cho, Synergistic Coupling of Metallic Cobalt Nitride Nano fi bers and IrO_x Nanoparticle Catalysts for Stable Oxygen Evolution, Chem. Mater. 30 (2018) 5941–5950, doi:10.1021/acs.chemmater.8b02061.

[61] M. Yu, Nitrogen-Doped Co3O4 Mesoporous Nanowire Arrays as an Additive-Free Air-Cathode for Flexible Solid-State Zinc–Air Batteries, Adv. Mater. 29 (15) (2017) 1–7, doi:10.1002/adma.201602868.

[62] Z. Xiao, Filling the oxygen vacancies in Co_3O_4 with phosphorus: An ultra-efficient electrocatalyst for overall water splitting, Energy Environ. Sci. 10 (12) (2017) 2563–2569, doi:10.1039/c7ee01917c.

[63] M. Dou, D. He, W. Shao, H. Liu, and F. Wang, "Pyrolysis of Animal Bones with Vitamin B12 : A Facile Route to Efficient Transition Metal – Nitrogen – Carbon (TM- N -C) Electrocatalysts for Oxygen Reduction," vol. 44106, pp. 2896–2901, 2016, doi: 10.1002/chem.201504983.

[64] D. Lynne, C. Kay, G. Dillard, Chairman \, Virginia Polytechnic Institute and State University, United State of America, 1982.

[65] D.M. Eby, K. Artyushkova, A.K. Paravastu, G.R. Johnson, Probing the molecular structure of antimicrobial peptide-mediated silica condensation using X-ray photoelectron spectroscopy, J. Mater. Chem. 22 (19) (2012) 9875–9883, doi:10.1039/c2jm30837a.

[66] A.R. Santos, R.K. Blundell, P. Licence, XPS of guanidinium ionic liquids: A comparison of charge distribution in nitrogenous cations, Phys. Chem. Chem. Phys. 17 (17) (2015) 11839–11847, doi:10.1039/c5cp01069a.

[67] W. Shi, W. Yang, Q. Li, S. Gao, P. Shang, J.K. Shang, The synthesis of nitrogen/sulfur co-doped TiO2 nanocrystals with a high specific surface area and a high percentage of {001} facets and their enhanced visible-light photocatalytic performance, Nanoscale Res. Lett. 7 (2012) 1–9, doi:10.1186/1556-276X-7-590.

[68] C.A. Lewis, R. Wolfenden, The nonenzymatic decomposition of guanidines and amidines, J. Am. Chem. Soc. 136 (1) (2014) 130–136, doi:10.1021/ja411927k.

[69] K. Zhao, H. Song, S. Zhuang, L. Dai, P. He, Y. Fang, Determination of nitrite with the electrocatalytic property to the oxidation of nitrite on thionine modified aligned carbon nanotubes, Electrochem. commun. 9 (1) (2007) 65–70, doi:10.1016/j.elecom.2006.07.001.

[70] A. Salimi, H. Mamkhezri, R. Hallaj, S. Soltanian, Electrochemical detection of trace amount of arsenic(III) at glassy carbon electrode modified with cobalt oxide nanoparticles, Sensors Actuators, B Chem 129 (1) (2008) 246–254, doi:10.1016/j.snb.2007.08.017.

[71] V. Sudha, S.A. Mohanty, R. Thangamuthu, Facile synthesis of Co_3O_4 disordered circular sheets for selective electrochemical determination of nitrite, New J. Chem. 42 (14) (2018) 11869–11877, doi:10.1039/c8nj02639d.

[72] A.J. Bard, L.R. Faulkner, Electrochemical methods: fundamentals and applications, 2nd ed., John Wiley & Sons, Inc., New York, 2001.

[73] H. Matsuda, Y. Ayabe, Zur Theorie der Randles-Sevčikschen Kathodenstrahl-Polarographie, Zeitschrift für Elektrochemie, Berichte der Bunsengesellschaft für Phys. Chemie 59 (6) (1955) 494–503.

[74] T. Islam, Fabrication of Ni–Co-Based Heterometallo-Supramolecular Polymer Films and the Study of Electron Transfer Kinetics for the Nonenzymatic Electrochemical Detection of Nitrite, ACS Appl. Polym. Mater. 2 (2) (2020) 273–284, doi:10.1021/acsapm.9b00797.

[75] E.M. Espinoza, Practical Aspects of Cyclic Voltammetry : How to Estimate Reduction Potentials When Irreversibility Prevails Practical Aspects of Cyclic Voltammetry : How to Estimate Reduction Potentials When Irreversibility Prevails *et al.*, 2019, doi:10.1149/2.0241905jes.

[76] C. Sandford*et al.*, "Chemical Science A synthetic chemist ' s guide to electroanalytical tools for studying reaction mechanisms," no. Cv, pp. 6404–6422, 2019, doi: 10.1039/c9sc01545k.

[77] M. Etesami, N. S. N. M. S. Chandran, M. H. Hussin, and A. Ripin, "Electrooxidation of Nitrite Ions on Gold /Polyaniline / Carbon Paste Electrode," vol. 11, pp. 8332–8345, 2016, doi: 10.20964/2016.10.32.
[78] T. Q. Nguyen and C. Breitkopf, "Determination of Diffusion Coefficients Using Impedance," vol. 165, no. 14, pp. 826–831, 2018, doi: 10.1149/2.1151814jes.
[79] L. Su, Surface reconstruction of cobalt phosphide nanosheets by electrochemical activation for enhanced hydrogen evolution in alkaline solution, Chem. Sci. 10 (7) (2019) 2019–2024, doi:10.1039/C8SC04589E.
[80] R. Tsuchida, Absorption Spectra of Co-ordination Compounds. II, Bull. Chem. Soc. Jpn. 13 (6) (1938) 436–450, doi:10.1246/bcsj.13.436.
[81] M.A. Rizvi, Complexation modulated redox behavior of transition metal systems (review), Rus. J. Gen. Chem. 85 (4) (2015) 959–973, doi:10.1134/S1070363215040337.
[82] Z. Zhao, Applied Surface Science Synthesis and electrochemical properties of Co_3 O_4-rGO /CNTs composites towards highly sensitive nitrite detection, Appl. Surf. Sci. 485 (2019) 274–282 January, doi:10.1016/j.apsusc.2019.04.202.
[83] A. Shrivastava, V. Gupta, Methods for the determination of limit of detection and limit of quantitation of the analytical methods, Chronicles Young Sci 2 (1) (2011) 21, doi:10.4103/2229-5186.79345.
[84] H.R. Zare, F. Memarzadeh, A. Gorji, M.M. Ardakani, Iodide-selective membrane electrode based on salophen complex of cobalt (III), J. Braz. Chem. Soc. 16 (3 B) (2005) 571–577, doi:10.1590/S0103-50532005000400013.
[85] W.J.R. Santos, Amperometric sensor for nitrite using a glassy carbon electrode modified with alternating layers of iron(III) tetra-(N-methyl-4-pyridyl)-porphyrin and cobalt(II) tetrasulfonated phthalocyanine, Talanta 70 (3) (2006) 588–594, doi:10.1016/j.talanta.2006.01.023.
[86] Y. Haldorai, J.Y. Kim, A.T.E. Vilian, N.S. Heo, Y.S. Huh, Y.K. Han, An enzyme-free electrochemical sensor based on reduced graphene oxide/Co_3O_4 nanospindle composite for sensitive detection of nitrite, Sensors Actuators, B Chem 227 (2016) 92–99, doi:10.1016/j.snb.2015.12.032.
[87] B. Agboola, T. Nyokong, Comparative electrooxidation of nitrite by electrodeposited Co(II), Fe(II) and Mn(III) tetrakis (benzylmercapto) and tetrakis (dodecylmercapto) phthalocyanines on gold electrodes, Anal. Chim. Acta 587 (1) (2007) 116–123, doi:10.1016/j.aca.2007.01.031.
[88] Z. Meng, B. Liu, J. Zheng, Q. Sheng, H. Zhang, Electrodeposition of cobalt oxide nanoparticles on carbon nanotubes, and their electrocatalytic properties for nitrite electrooxidation, Microchim. Acta 175 (3–4) (2011) 251–257, doi:10.1007/s00604-011-0688-y.
[89] L. Lu, Highly sensitive detection of nitrite at a novel electrochemical sensor based on mutually stabilized Pt nanoclusters doped CoO nanohybrid, Sensors Actuators, B Chem 281 (2019) 182–190, doi:10.1016/j.snb.2018.10.074.
[90] S. Lu, C. Yang, M. Nie, Hydrothermal synthesized urchin-like nickel-cobalt carbonate hollow spheres for sensitive amperometric detection of nitrite, J. Alloys Compd. 708 (2017) 780–786, doi:10.1016/j.jallcom.2017.03.059.
[91] L. Cui, T. Pu, Y. Liu, X. He, Layer-by-layer construction of graphene/cobalt phthalocyanine composite film on activated GCE for application as a nitrite sensor, Electrochim. Acta 88 (2013) 559–564, doi:10.1016/j.electacta.2012.10.127.
[92] A.S. Adekunle, J. Pillay, K.I. Ozoemena, Probing the electrochemical behaviour of SWCNT-cobalt nanoparticles and their electrocatalytic activities towards the detection of nitrite at acidic and physiological pH conditions, Electrochim. Acta 55 (14) (2010) 4319–4327, doi:10.1016/j.electacta.2009.02.102.
[93] S. Lu, M. Hummel, S. Kang, Z. Gu, Selective Voltammetric Determination of Nitrite Using Cobalt Phthalocyanine Modified on Multiwalled Carbon Nanotubes, J. Electrochem. Soc. 167 (4) (2020) 046515, doi:10.1149/1945-7111/ab7982.
[94] P. Li, Self-assembly of tetrakis (3-trifluoromethylphenoxy) phthalocyaninato cobalt(II) on multiwalled carbon nanotubes and their amperometric sensing application for nitrite, ACS Appl. Mater. Interfaces 5 (6) (2013) 2255–2260, doi:10.1021/am400152k.
[95] R.M. Abdel Hameed, S.S. Medany, Evaluation of core-shell structured cobalt@platinum nanoparticles-decorated graphene for nitrite sensing, Synth. Met. 247 (November 2018) 67–80, doi:10.1016/j.synthmet.2018.11.011.
[96] J. Wang, N. Hui, A nanocomposite consisting of flower-like cobalt nanostructures, graphene oxide and polypyrrole for amperometric sensing of nitrite, Microchim. Acta 184 (7) (2017) 2411–2418, doi:10.1007/s00604-017-2247-7.
[97] B.S. Jilani, P.Malathesh Mounesh, C.D. Mruthyunjayachari, K.R.V. Reddy, Cobalt (II) tetra methyl-quinoline oxy bridged phthalocyanine carbon nano particles modified glassy carbon electrode for sensing nitrite: A voltammetric study, Mater. Chem. Phys. 239 (2020) 121920 August, doi:10.1016/j.matchemphys.2019.121920.
[98] V. Sudha, K. Krishnamoorthy, S.M. Senthil Kumar, R. Thangamuthu, Copper oxide nanosheet modified electrodes for simultaneous determination of environmentally hazardous anions, J. Alloys Compd. 764 (2018) 959–968, doi:10.1016/j.jallcom.2018.06.077.
[99] V. Sudha, S.M. Senthil Kumar, R. Thangamuthu, Simultaneous electrochemical sensing of sulphite and nitrite on acid-functionalized multi-walled carbon nanotubes modified electrodes, J. Alloys Compd. 749 (2018) 990–999, doi:10.1016/j.jallcom.2018.03.287.
[100] M. Shivakumar, K.L. Nagashree, S. Manjappa, M.S. Dharmaprakash, Electrochemical Detection of Nitrite Using Glassy Carbon Electrode Modified with Silver Nanospheres (AgNS) Obtained by Green Synthesis Using Pre-hydrolysed Liquor, Electroanalysis 29 (5) (2017) 1434–1442, doi:10.1002/elan.201600775.